Cytoplasmic flows as signatures for the mechanics of mitotic positioning

Ehssan Nazockdast[a,b,*], Abtin Rahimian[b], Daniel Needleman[c], and Michael Shelley[a,b,*]
[a]Center for Computational Biology, Flatiron Institute, New York, NY 10010; [b]Courant Institute of Mathematical Sciences, New York University, New York, NY 10012; [c]School of Engineering and Applied Sciences, Harvard University, Cambridge, MA 02138

ABSTRACT **The proper positioning of mitotic spindle in the single-cell *Caenorhabditis elegans* embryo is achieved initially by the migration and rotation of the pronuclear complex (PNC) and its two associated astral microtubules (MTs). Pronuclear migration produces global cytoplasmic flows that couple the mechanics of all MTs, the PNC, and the cell periphery with each other through their hydrodynamic interactions (HIs). We present the first computational study that explicitly accounts for detailed HIs between the cytoskeletal components and demonstrate the key consequences of HIs for the mechanics of pronuclear migration. First, we show that, because of HIs between the MTs, the cytoplasm-filled astral MTs behave like a porous medium, with its permeability decreasing with increasing the number of MTs. We then directly study the dynamics of PNC migration under various force-transduction models, including the pushing or pulling of MTs at the cortex and the pulling of MTs by cytoplasmically bound force generators. Although achieving proper position and orientation on reasonable time scales does not uniquely choose a model, we find that each model produces a different signature in its induced cytoplasmic flow. We suggest that cytoplasmic flows can be used to differentiate between mechanisms.**

Monitoring Editor
Alex Mogilner
New York University

Received: Mar 14, 2016
Revised: Feb 27, 2017
Accepted: Mar 16, 2017

INTRODUCTION

The cytoskeleton is an ensemble of filaments and molecular motors immersed in the cytoplasmic fluid and is involved in cellular processes such as cell division and migration. The energy required for the rearrangement of cytoskeletal components and organelle transport is typically provided by the force exchange between the cytoskeletal filaments—including microtubules (MTs) and actin fibers—and motor proteins. These interactions are local, that is, they occur over the length scales of the molecular motors, which are significantly smaller than the length of the filaments. Nevertheless, because the structures are embedded in the cytoplasmic fluid, their motion can instantaneously induce flows on the scale of the cell (Shelley, 2016). These *nonlocal* interactions between the cytoplasmic fluid and the structures within (fibers, nuclei, the cell cortex, etc.) are referred to as hydrodynamic interactions (HIs). Previous theoretical and computational studies of the mechanics of cytoskeleton mostly ignore HIs, often arguing that HIs are *screened* in the dense network/suspension of filaments (Broedersz and MacKintosh, 2014). The purpose of this work is to revisit this assumption and use detailed simulations to demonstrate the importance of HIs in determining the mechanics of cytoskeletal assemblies.

For this purpose, we developed a versatile and highly efficient numerical platform for studying the dynamics of active and flexible filaments in cellular assemblies (Nazockdast *et al.*, 2017). This method offers a major improvement from our earlier numerical study (Shinar *et al.*, 2011), which did not explicitly model HIs between MTs and their mechanical flexibility. This is, to our knowledge, the first attempt to incorporate many-body HIs between MTs and other intracellular bodies with the cytoplasmic fluid while also accounting for the flexibility of MTs, their dynamic instability, and interactions with motor proteins. By accounting for HIs, we can also compute the large-scale cytoplasmic flows generated by the movements of MTs and other immersed bodies within the cell.

This article was published online ahead of print in MBoC in Press (http://www.molbiolcell.org/cgi/doi/10.1091/mbc.E16-02-0108) on March 22, 2017.

*Address correspondence to: Ehssan Nazockdast (enazockdast@simonsfoundation.org), Michael Shelley (mshelley@simonsfoundation.org).

Abbreviations used: AP, anterior–posterior; HIs, hydrodynamic interactions; MTs, microtubules; PNC, pronuclear complex.

Supplemental Material can be found at:
http://www.molbiolcell.org/content/suppl/2017/03/20/mbc.E16-02-0108v1.DC1

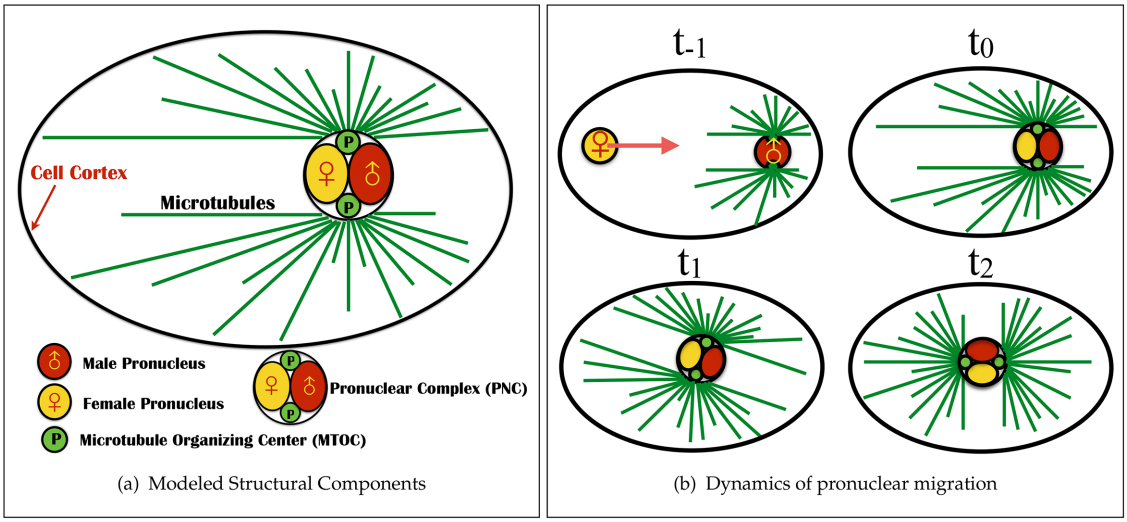

FIGURE 1: The modeled structural components and dynamics of pronuclear migration in the single-cell *C. elegans* embryo. (a) Structural components. The pronuclear complex—here modeled as a rigid sphere—contains the male (red) and female (yellow) pronuclei and is attached to two arrays of MTs (green lines) that polymerize from two centrosomes (green bodies). These structures are immersed in the cellular cytoplasm (light blue) and confined within an ellipsoidal eggshell. (b) The dynamics of pronuclear migration and positioning. At $t = t_{-1}$, the female pronucleus moves to the posterior to combine with the male pronucleus ($t = t_0$) to form the PNC. This initial period of female nuclear migration is not modeled here (Payne *et al.*, 2003). Between $t = t_0$ and t_1, the PNC moves anteriorwise to the center while rotating into "proper position" with the centrosomal axis along the AP axis ($t = t_2$).

As an example, we study pronuclear migration before the first cell division of the *Caenorhabditis elegans* embryo (see the schematic in Figure 1). Proper positioning of the mitotic spindle is indispensable to the successful segregation of chromosomes and to the generation of cell diversity in early development (Cowan and Hyman, 2004). Before mitosis and after fertilization, the female pronucleus migrate toward (at $t = t_{-1}$ in the schematic) and meets the male pronucleus ($t = t_0$) and its associated astral array of MTs at the cell posterior to form the pronuclear complex (PNC). The PNC then moves toward and centers at the cell center ($t = t_1$) and rotates 90° ($t = t_2$) to align the axis between its two associated centrosomes with the cell's anterior–posterior (AP) axis. The mitotic spindle then forms, and the chromatid pairs are pulled toward the opposite sides of the cell ($t > t_2$).

HIs arise from several features of PNC migration. Centering and rotating the PNC will push and rotate the cytoplasm, as well as the astral MT arrays. Hence each structure moves against the backdrop of flows produced by the other. Further, because the PNC and its associated MT arrays are on the scale of the cell itself, the confinement of the cell will have a very strong effect on the nature of the cytoplasmic flows. Finally, as we will show, the mechanisms of force transduction that position the PNC can have a qualitative—and in principle experimentally measurable—effect on these flows.

To start, we study the flow induced by the motion of the PNC and its attached astral MTs, irrespective of the force transduction mechanisms. For this, we perform the numerical experiment of pulling the PNC, and its astral MT array, with an externally applied force from the posterior to the center of the cell and aligning it with AP axis with an externally applied torque. By studying the resulting flows, we establish, as a consequence of HIs, that the cytoplasm-filled astral MTs behave like a porous medium surrounding the PNC, where the permeability of the medium decreases with increasing number of MTs. To quantify the effect of HIs, we compare the computed translational and rotational drag on the PNC/MT-array complex with other estimates, including those based on the radius of the aster formed by the MTs (Reinsch and Gönczy, 1998; Kimura and Onami, 2005, 2007), those using a local drag model (Nedelec and Foethke, 2007), and our previous study, which ignored the MT drag altogether (although not PNC drag or the effect of confinement; Shinar *et al.*, 2011). We find in each case that these estimates drastically overestimate or underestimate this drag by a large factor. We also find that confinement has a much stronger effect on translational than on rotational drag, meaning that HIs cannot be lumped into a modified viscosity.

We next establish that the cytoplasmic flows induced by HIs can be used as a diagnostic tool to differentiate between different active mechanisms for pronuclear migration. For this, we instantiate three proposed mechanisms for pronuclear migration in *C. elegans*. 1) The *cortical pulling* model, in which MTs impinging on the cortex are pulled on by dynein motors that are attached to the plasma membrane, in particular by association to the protein complex formed by the Gα subunits, GPR-1/2, and LIN-5. An asymmetric distribution of PAR and LET-99 proteins on the cortex in prophase then produces an asymmetric association of dyneins with the protein complex and larger pulling forces on the anterior, and so the pronuclear complex moves in that direction (Grill *et al.*, 2001; Tsou *et al.*, 2002; Labbé *et al.*, 2004; Goulding *et al.*, 2007; Kimura and Onami, 2007; Siller and Doe, 2009; McNally, 2013). 2) The *cortical pushing* model, in which the growth of astral MTs against the cell periphery induces repulsive forces on MTs that move the complex away from the periphery and thus opens space for further polymerization (Holy *et al.*, 1997; Reinsch and Gönczy, 1998; Tran *et al.*, 2001). Perhaps the strongest evidence in support of the cortical pushing mechanism being involved in the positioning of the mitotic spindle in *C. elegans* comes from the recent study by Garzon-Coral *et al.* (2016), in which the magnetic tweezers are used to directly measure the forces involved in the positioning of the mitotic spindle. Using these force measurements in different molecular and geometrical perturbations,

Garzon-Coral *et al.* (2016) argue that the cortical pushing forces maintain the position of the mitotic spindle during metaphase. 3) The *cytoplasmic pulling* model, in which forces are applied by cargo-carrying dyneins attached on MTs and walking toward the centrosomes (Kimura and Onami, 2007). As a consequence of Newton's third law, the force applied by dynein on MTs is equal and opposite to the force required to move the cargo through the cytoplasm (Shinar *et al.*, 2011; Longoria and Shubeita, 2013). Because longer MTs carry more dyneins and produce larger pulling forces, the PNC moves in the direction of longer MTs, that is, anteriorwise.

First, we show that all three mechanisms can center and rotate the PNC on a reasonable time scale, and so proper positioning alone cannot choose a unique model. However, we demonstrate that each mechanism produces its own *fingerprint* in the generated cytoplasmic flows, which can be used to differentiate between them. These flow signatures are generic features of each mechanism and do not depend on the details of its biochemical regulation and molecular pathways. Specifically, we show that the cytoplasmic flow generated in the cortical pulling model is analogous to the flow that arises from pushing a porous object with an external force. In the cortical pushing model, the cytoplasmic flow is the combination of that same driven porous object flow with that produced by MT deformations induced by compressive polymerization forces at the periphery. Finally, we demonstrate that the flow induced by a cytoplasmic pulling model is fundamentally different because it can be interpreted as a porous structure that is moved by internal force generators, with its early time flows in the class of *self-propelled puller particles* (Saintillan and Shelley, 2013).

Although this study focuses on the pronuclear migration process in the *C. elegans* embryo, the active mechanisms discussed here, including the polymerization forces and forces from cortically or cytoplasmically bound dyneins, are used in other stages of cell division and in other organisms (Howard, 2001). Thus the generic features of these mechanical models, including their flow signatures, can be useful in identifying or differentiating between force transduction mechanisms in other instances.

RESULTS

A few remarks on the scale of single-microtubule drags and flows

The microscopic size of subcellular structures and the large viscosity of cytoplasm yield inertial forces of the cytoplasm negligible compared with viscous forces. Assuming for simplicity that the response of the cytoplasm is Newtonian, we find the force balance in the fluid phase to be governed by the incompressible Stokes equations (Happel and Brenner, 1965):

$$\mu\nabla^2 u - \nabla p = 0, \quad \nabla\cdot u = 0 \tag{1}$$

where μ is the viscosity of the cytoplasm and u and p are the fluid velocity and pressure fields, respectively. Owing to the linearity of the Stokes equation, the induced velocity of the PNC is related to the net force on it by an instantaneous drag coefficient, γ, of the structure composed of the PNC and its attached astral MTs.

An important consequence of being in the Stokesian regime is that the drag coefficients of the immersed objects scale with their longest dimensions, making the drag of very thin individual MTs nonetheless comparable to the drag on the PNC. To see this, consider an MT of length $L = 10$ µm, which is about the diameter of the PNC and on the scale of astral MT lengths, being moved transversely to itself at a constant speed, U. Slender body theory (Tornberg and Shelley, 2004) estimates the drag force on the MT as $F = 8\pi\mu LU / \ln\left(\epsilon^{-2}e^{-1}\right)$, where ϵ is the aspect ratio of the MT (~1/400). The classical Stokes formula estimates the drag force on a spherical PNC moving at the same speed and diameter L as $F = 3\pi\mu LU$. The ratio of these two drags (MT to PNC) is given by $(8/3)\ln^{-1}(\epsilon^{-2}e^{-1}) \approx 0.25$. Hence, despite having a diameter of only 24 nm, a single MT has 25% of the PNC's drag. This can be seen more clearly by noting that the drag coefficient has only a weak logarithmic dependence, $\ln^{-1}(\epsilon^{-2}e^{-1})$, on the thickness of the MT.

The large drag of a single MT is associated with the large volume of fluid that is transported by the motion of that MT. To visualize this long-range nature of the induced flows, in Figure 2a we show the fluid velocity vectors around a single fiber (thick black line) being pulled in the transverse direction and the variations of the magnitude of the fluid velocity induced by this motion. The generated flow is three dimensional, but for visualization, we present only the results in the plane of the fiber (and of the force). The solid white line is the contour line that corresponds to $|\boldsymbol{u}| = 0.20U$, where $|\boldsymbol{u}|$ is the magnitude of the induced fluid velocity. We can see that at distances comparable to the length of the MT, the fluid velocity remains significant. In other words, as long as the separation distance between the astral MTs is less than or comparable to their length, as it typically is in cytoskeletal assemblies, the motion of an individual MT is strongly coupled to the other MTs through the cytoplasmic flows.

Cytoplasm-filled astral microtubules behave as a porous medium

The mechanical role of astral MTs in all three pronuclear positioning mechanisms is to transfer the force applied either on their plus ends (by cortical pushing or pulling) or along their lengths (by cytoplasmic pulling) to their minus ends anchored in the centrosomes, themselves attached to the PNC. This results in active forces and torques acting on the PNC. Thus the feature of the cytoplasmic flow that is common in all of the cortically based mechanisms—the cortical pushing and cortical pulling mechanisms—is the flow generated by the motion of the PNC and its anchored astral MTs under a given

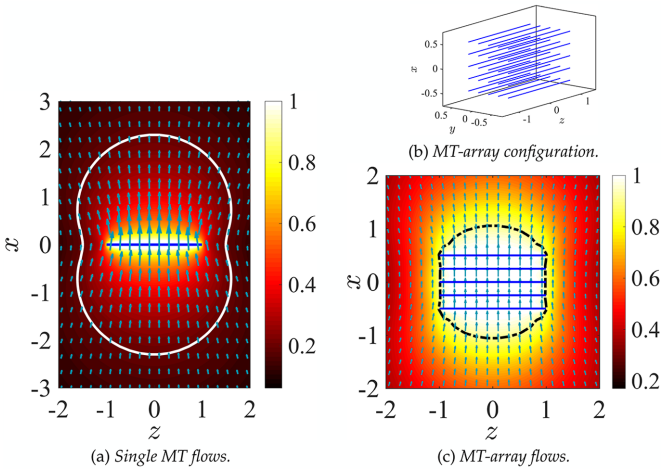

FIGURE 2: The 3D cytoplasmic flow induced by moving (a) a single MT and (c) a MT array in their transverse direction (x-axis) and with a net velocity $U = 1$, projected in the plane of the motion of the MT xz-plane. The arrows show the fluid velocity vectors. The size of the arrows and the background color plots correspond to the local magnitude of the fluid velocity. (b) The 3D configuration of the MT array. The solid white line in a corresponds to the contour with velocity magnitude $|u| = 0.20U$. The dark dashed line in c is the contour with $|u| = 0.90U$, roughly corresponding to the effective hydrodynamic size of the MT array.

	Drag on MT array without HIs	Drag on MT array with HIs
3×3	2.25	0.63
5×5	6.25	0.66
10×10	25	0.68
15×15	56.25	0.68

The values are normalized by the drag on a sphere with a diameter equal to the length of the MTs in the array.

TABLE 1: Predicted drag on the MT-array, γ_{array}, in the presence and absence of HIs.

external force and/or torque. To understand the effect of HIs between MTs, we first study the flow induced by a much simpler MT assembly: a 5×5 microtubule array that moves with velocity $U = 1$ along the transverse direction of MTs (x-axis) in free space (Figure 2b). Figure 2c shows the resulting fluid velocity field and the spatial variations of its magnitude in the xz-plane. Again, the fluid flow is three dimensional, and the results are projected into the xz-plane for visualization. The enclosed surface illustrated by a dashed line is the fluid velocity magnitude contour corresponding to $|\boldsymbol{u}| = 0.9U$. Hence those fluid elements within this surface move roughly with the velocity of the MT array. In other words, HIs between the MTs significantly reduce the convective penetration of the fluid between the MTs and result in an effective hydrodynamic surface that is much larger than the total surface area of all MTs. The microtubule array, therefore, can be seen as a porous volume in which the fluid permeability is decreased as more MTs are included in the array. The HIs also affect the drag on the MT array. As we showed earlier, the drag of a single MT moving transversely is roughly 1/4 of a sphere with the same diameter as the MT length, $\gamma_{MT} = 0.25\ \gamma_{sph}$. If HIs are neglected, the total drag on the MT array is the summation of the drag on the individual MTs: $\gamma_{array} = 5 \times 5 \times 0.25\ \gamma_{sph} = 6.25\ \gamma_{sph}$. However, when HIs are accounted for, the computed drag of the MT array is only $\gamma_{array} = 0.66\ \gamma_{sph}$, which is ~10 times smaller than the local drag prediction. Of interest, increasing the number of MTs in the array to 10×10 increases the total drag by <4%, to $\gamma_{array} = 0.68\ \gamma_{sph}$. The computed drag for a 15×15 remains almost unchanged from that for a 10×10 array, as if the entire volume in the MT array was filled with MTs. Note that if HIs are ignored, the predicted drag for 15×15 MT-array is $\gamma_{array} = 56.2\ \gamma_{sph}$, which is ~85 times larger than the computed value; see Table 1.

With that in hand, we now explore the flows generated by translation and rotation of the PNC and its associated astral MT arrays, first by pulling it with a given external force from the cell posterior to its center, and then rotating it to proper alignment by applying an external torque. The resulting flows are illustrated in Figure 3 using $N_{MT} = 600$ astral MTs. Flows in the absence of astral MTs are also shown for comparison. Again, the flow is three dimensional and is projected to the plane of the applied force and AP axis to aid visualization. The simulation parameters are given in Table 2. Two main translational flow features that are apparent in the presence and the absence of MTs are 1) fluid flows in the direction of motion of the PNC and along the AP axis, and 2) reversed flows induced by cellular confinement. Comparing Figure 3a and Figure 3b shows that the presence of the MT array reduces the size of the reversing flow zone. In other words, the presence of MTs increased the effective hydrodynamic radius of the PNC (dashed circle). This increase in hydrodynamic radius is also apparent in rotational motion (Figure 3, c and d) by noting that the magnitude of the bulk velocity decays much more slowly away from the PNC when the astral MTs are present.

We observed the same trend in the earlier example of MT arrays (Figure 2c), which can be described as follows. In pronuclear migration, the astral MTs act as a comoving porous layer that surrounds the PNC and abuts the cell periphery. In particular, the HIs between the MTs reduce the convective penetration of fluid into the porous layer and creates an effectively larger object moving through (or rotating in) the fluid. Note that the relevant dimension of MTs that defines the strength of HIs and the fluid flow into the astral MTs is the length of the MTs and not their thickness. Thus, as we saw in the earlier example of the MT array, a small number of astral MTs can substantially increase the effective volume of the PNC and reduce the permeability of the fluid into the volume filled with astral MTs. See Nazockdast *et al.* (2017) for a more quantitative study of the cytoplasm-filled astral MTs behaving as a porous medium.

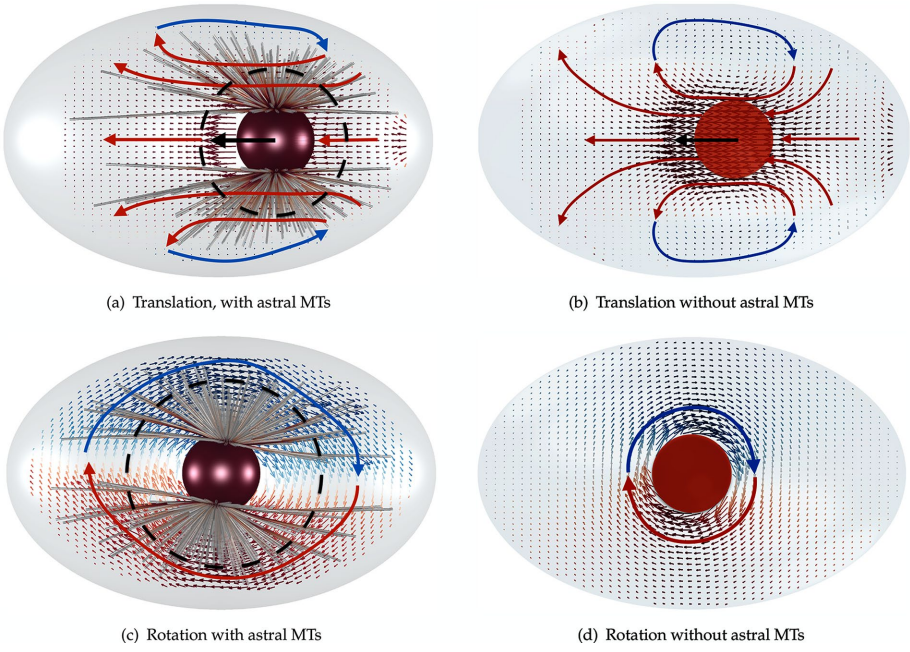

FIGURE 3: The cytoplasmic flows induced by (a) translational and (c) rotational motion of the PNC and its attached astral MTs. (b, d) Translational and rotational flows in the absence of astral MTs.

Neglecting hydrodynamic interactions produces wrong estimates of pronuclear migration force magnitudes

To provide a more quantitative analysis of the effect of the astral MTs on the dynamics of pronuclear migration, we compute the translational, $\gamma_T = F/U_{PNC}$, and rotational, $\gamma_R = F/\Omega_{PNC}$, drag coefficients as a function of the number of MTs. Here U_{PNC} and Ω_{PNC} are the computed translational and angular velocities of the PNC under external force F and torque T, respectively. We consider three different conditions or models. In model 1, we neglect all HIs and calculate drag on MTs using a local slender-body drag

Parameter	Value used in simulations
MT growth velocity (V_g^0)	0.12 μ·s^{-1}
MT shrinkage velocity (V_s)	0.288 μ·s^{-1}
MT rate of catastrophe (f_{cat}^0)	0.014 μ·s^{-1}
MT rate of rescue (f_{res})	0.014 μ·s^{-1}
MT bending modulus (E)	10 pN·m^2
MT stall force for polymerization reaction (F_S^P)	4.4 pN
Cytoplasmic dynein's stall force (F^{stall})	1 pN
Viscosity of the cytoplasm (μ)	1 pa·s
Long axis of the cell	50 μm
Short axis of the cell	30 μm
Radius of the pronuclear complex (α_{PNC})	5 μm

These values are taken from Table 1 of Kimura and Onami (2005). The references related to each measurement are given in that article.

TABLE 2: The biophysical parameters used in our simulations.

formula (Tornberg and Shelley, 2004) and drag on the PNC using Stokes' drag formula. This approximation closely follows the Brownian dynamics simulation techniques used for modeling cellular assemblies, such as Cytosim (Nedelec and Foethke, 2007). In model 2, we include HIs among the MTs and with the PNC but neglect the backflow generated by the cell periphery through the no-slip boundary condition. That is, in model 2, cytoplasm flows in and out of the cell periphery without impedance. The confining presence of the cell wall is partially maintained by having MTs depolymerize upon reaching it. In model 3, we include all HIs—in particular, those that arise from applying the no-slip boundary condition at the periphery. A comparison between models 2 and 3 model allows us to separate the effect of confinement flows induced by the cell wall from those induced by the aster.

Figure 4 shows the variation of computed translational and rotational drag coefficients with the number of MTs for models 1–3. The values are normalized, respectively, by the drag coefficients of a rigid spherical PNC, $\gamma_T^0 = 6\pi\mu R_{PNC}$ and $\gamma_R^0 = 6\pi\mu R_{PNC}$. The black reference lines at $\hat{\gamma}_T = \gamma_T/\gamma_T^0 = 2$ and $\hat{\gamma}_R = \gamma_R/\gamma_R^0 = 8$ are estimates that assume that PNC drag can be modeled using Stokes' formula with an effective sphere of radius $R = 2R_{PNC}$, as used by Kimura and Onami (2005, 2007) in their modeling of pronuclear rotation and centering.

As expected for model 1, having no HIs between MTs, both drag coefficients increase linearly with N_{MT}, showing no saturation. For model 2, $\hat{\gamma}_{R,T}$ increases monotonically with N_{MT}, with $\hat{\gamma}_T$ saturating as $N_{MT} \to \infty$ This behavior can be explained through our earlier finding that the astral MTs and cytoplasm form a porous medium. As the number of MTs is increased, the permeability of the porous medium is decreased, while the effective hydrodynamic dimensions of the PNC are increased. In the limit of $N_{MT} \to \infty$ the flow cannot penetrate the porous layer, which fills the cell volume. Because in model 2 the back flows induced by the cell confinement are neglected, in this limit, the drag coefficients asymptote to those of a solid object filling the cell and moving in free space.

When confinement-induced back flows are included by accounting for HIs with the periphery (model 3), the drag coefficients again show monotonic increase with N_{MT}. However, for $N_{MT} = 1200$, the $\hat{\gamma}_T$ of model 3 is sixfold larger than that for model 2, severalfold smaller than for model 1, and sixfold smaller than for model 3 with $N_{MT} = 0$ (the red star), which corresponds roughly to our previous modeling (Shinar *et al.*, 2011) of pronuclear migration in which MT drag was not included. Now, as $N_{MT} \to \infty$, the effective hydrodynamic dimensions of PNC approaches the size of cell periphery, and we expect $\hat{\gamma}_T \to \infty$ due to the no-slip condition.

Rotational dynamics of the PNC

Figure 4b shows that the rotational drag coefficient qualitatively follows the same trend as the translational coefficient, with one key difference. Comparing models 2 and model 3 in Figure 4, a and b, shows that confinement has a much smaller effect on the dynamics of rotation than on translational motion. This is expected because rotation of the PNC and the astral MTs involves sliding an effectively larger PNC tangentially to the cell periphery, whereas translation involves moving the effective surface of the PNC and the astral MTs normal to the cell periphery's surface, which induces larger resistance to motion (Happel and Brenner, 1965).

We can use the predictions of model 2, shown in Figure 4, a and b, to study a more fundamental question: can the mixture of cytoplasm and astral MTs be modeled as a fluid with a simple effective viscosity? If that is true, then we expect the ratios of the translational drag coefficient to the rotational drag coefficient to be independent of the number of MTs i.e., $\hat{\gamma}/\hat{\gamma}_T = 1$. Our model 2 predictions, however, show that $\hat{\gamma}/\hat{\gamma}_T$ increases from 1 at $N_{MT} = 0$ to 7 at $N_{MT} = 1200$. This simple example demonstrates that HIs cannot be coarse grained through a single effective viscosity because HIs do not have the same dynamical effect on rotational and translational motions. Instead, our simulations show generally that the entire cytoplasm-filled MT array acts as a porous medium whose permeability decreases with increasing number of MTs, thus

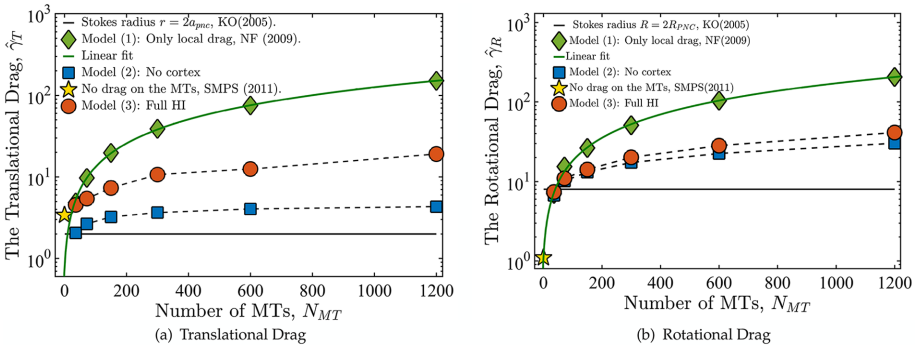

FIGURE 4: (a) Normalized translational, $\hat{\gamma}_T = \gamma_T/\gamma_T^0$, and rotational, $\hat{\gamma}_R^0 = \gamma_R/\gamma_R^0$, drag coefficients vs. number of MTs, where $\gamma_T^0 = 6\pi\mu R_{PNC}$ and $\gamma_R^0 = 8\pi\mu R_{PNC}^3$ are the translational and rotation drag coefficients, respectively, of a rigid spherical PNC in the absence of MTs. The solid straight lines correspond to the estimates used in Kimura and Onami (2005, 2007); ◊, predictions of model 1, in which only the local drag coefficient of individual MTs is accounted for, as used by Cytosim (Nedelec and Foethke, 2007); □, predictions of model 2, in which HIs with the cell cortex (hydrodynamic confinement) is neglected; *, our previous study, which neglects the drag on the MTs (Shinar *et al.*, 2011); ○, simulation result of model 1, which fully accounts for all HIs. The solid lines going through the prediction of model 2 are linear fits to the data. These equations are $\hat{\gamma}_T = 1 + 0.12\ N_{MT}$ and $\hat{\gamma}_R = 1 + 0.17\ N_{MT}$ for translational and rotational drag, respectively.

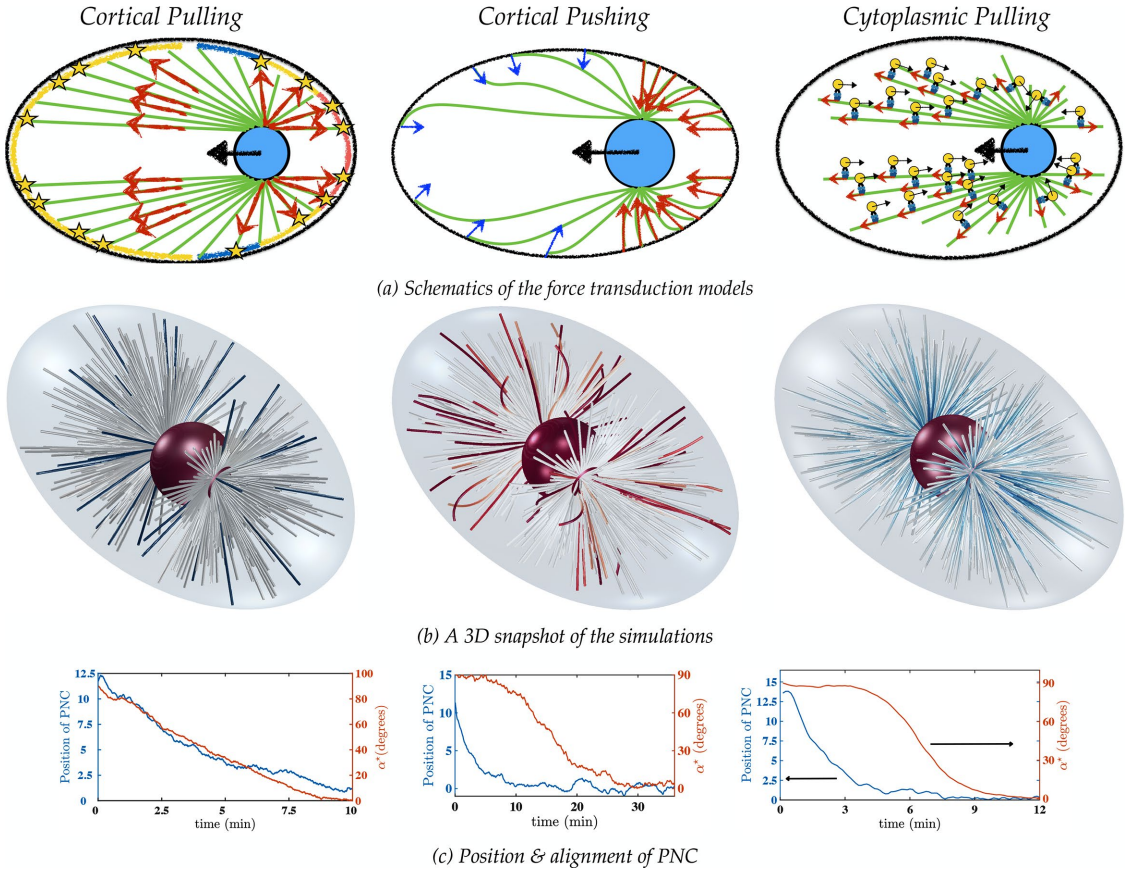

FIGURE 5: (a) The force transduction mechanisms. Left, cortical pulling model, in which the blue, yellow and red strips on the cortex correspond to the lowest, average, and highest density, respectively, of the cortical force generators. See the Supplemental Materials for details. Middle, the cortical pushing model. The larger number of MTs polymerizing against the cortex on the posterior side and their shorter lengths (corresponding to larger bending forces) result in larger pushing forces on the posterior pole (compared with the anterior) and pronuclear migration from posterior to the center of the cell. Right, the length-dependent cytoplasmic pulling mechanism, in which cargo-carrying dynein motors apply pulling forces on the astral MTs. Longer MTs have more dyneins attached to them, which result in pronuclear migration toward the longest MT, that is, from posterior to the center of the cell. (b) Long-time 3D snapshots of the simulations in the three mechanisms (Supplemental Movies S1–S3). The fibers are color coded with respect to the local tension; red, blue, and white denote compressional, extensional, and no forces, respectively. In the cortical and cytoplasmic pulling models, the MTs are under extensile forces and thus remain straight; in the cortical pushing simulations, the MTs are buckled due to the compressional forces from their polymerization against the cortex. (c) Variations of the PNC position and angle between the intercentrosomal axis and the AP axis vs. time.

giving an increased effective size of the PNC in response to an applied force (at least in the absence of force generators within the astral MT array producing active flows). The different scaling of translational and rotational drag coefficients with the effective radius of the PNC (γ_T scales with R, whereas γ_R scales with R^3) causes $\hat{\gamma}_R/\hat{\gamma}_T \sim R^2$ to increase, as the effective radius of the PNC and its astral MTs increases with the number of MTs.

Three mechanisms of pronuclear migration yield proper positioning of the pronuclear complex

We now investigate the mechanics of pronuclear migration and positioning using three proposed positioning mechanisms in *C. elegans* embryo; namely the cortical pulling, cortical pushing, and cytoplasmic pulling models. To start, within our framework, we instantiated a cortical pulling model that Kimura and Onami (2007) developed for their study of pronuclear migration. Figure 5a shows a schematic of this model, which was motivated by experimental observations of Tsou *et al.* (2002). In this model, pulling forces on astral MTs are generated by the asymmetric attachment of astral MTs to cortically bound dyneins, whose activation probability is inhomogeneously distributed along the posterior cortex, with the greatest probability of attachment at the posterior pole and the least to the immediate posterior of the midplane. Attached MTs are pulled upon, and simultaneously depolymerized, at the cortex; see the Supplemental Materials for details. A snapshot of the simulation at long times is shown in Figure 5b, left. It demonstrates that this mechanism leads to centering and rotation to the proper position. In this simulation, PNC translation and rotation are in temporal register, and proper position is achieved on a reasonable time scale (Figure 5c, left). Because the cortically bound force generators in this model put the MTs under an extensional load, MT deformations are small and remain relatively straight (Figure 5b, left). For the parameters used in this simulation (motor attachment distribution and number density, MT attachment and detachment rates, etc.),

we find that the PNC robustly finds the proper position. These chosen parameters were physiologically reasonable but also narrowly constrained, as other, seemingly reasonable choices of these parameters can lead to lack of centering. More details are given in the Supplemental Materials; the biophysical parameters corresponding to the figures are given in Table 2.

Next we consider a variation of the cortical pushing model. In this model, we constrain the position of the MT plus ends, which reach and polymerize at the cortex to remain fixed (and hinged) at the cortex as long as they are in growing state (see the Supplemental Materials). In an idealized system in which the PNC is pushed by an up–down symmetric set of astral MTs, the intercentrosomal axis would remain orthogonal to the AP axis throughout the centering process (having started that way). However, a combination of dependence of polymerization forces on MT length (shorter MTs are harder to deform, resulting in larger polymerization forces) and the elongated shape of the cell periphery makes this orientation mechanically unstable and susceptible to the fluctuations that MT dynamic instability can provide. Once seeded, this "torque instability" produces a self-reinforcing, rotating torque on the PNC, moving it toward the proper position, which is a mechanically stable equilibrium (see the Supplemental Materials).

As shown in Figure 5c, middle, this model results in proper centering and rotation of the PNC on a reasonable time scale. In addition, Figure 5b, middle, shows that for this particular instantiation of the cortical pushing model, the MTs are substantially buckled near the cortex. We also considered another variation of cortical pushing in which, rather than fixing the plus ends of MTs, pushing forces are applied in the normal direction to the cell boundary (pointing inward) so that MT plus ends cannot penetrate the boundary. MTs are nonetheless allowed to grow or slide freely tangentially. Our simulations show that, although the PNC properly centers in this model, it fails to rotate the PNC to the proper alignment with the AP axis; this variation of the model is discussed in detail in the Supplemental Materials.

Finally, Figure 5a, right, shows a schematic of the cytoplasmic pulling model. This model was initially proposed to explain observations in newly fertilized sand-dollar eggs (Hamaguchi and Hiramoto, 1986). Later, via modeling and experimental study, this was proposed as a mechanism for pronuclear positioning in the *C. elegans* embryo (Kimura and Onami, 2005; Kimura and Kimura, 2011). This model was studied in our earlier work on pronuclear migration (Shinar *et al.*, 2011), in which minus end–directed cargo-carrying dyneins walk on MTs and thus apply a pulling force on them toward their plus end. Applying proper force balance (Shinar *et al.*, 2011), the cargo exerts an equal and opposite force on the fluid. If dyneins are uniformly distributed along the MTs, as is assumed here, the PNC moves in the direction of the longest MTs, as these contribute the greatest pulling forces; see the Supplemental Materials for details. As shown in Figure 5c, right, this model can yield both centering and rotation on a time-scale comparable to experimental observations (Kimura and Onami, 2005). Similarly to the cortical pulling model, the MTs are under extension, and their deformations are small, which is evident in the long-time three-dimensional (3D) snapshot of the simulation in Figure 5b, right.

Cytoplasmic flows during pronuclear migration

Our simulation results thus far show that all three positioning mechanisms can produce the expected alignment and position of the pronuclear complex within a reasonable time scale and choice of biophysical parameters. We now discuss their induced cytoplasmic flows and the generic features specific to each. Our motivation is that different mechanisms of force transduction will exert different forces on MTs and hence should be associated with generically different cytoplasmic flows. To demonstrate these differences, we start by studying the flows induced by a single MT growing against a barrier and by a single cargo-carrying dynein motor walking along a MT. These are the simplest representations of cortical pushing and cytoplasmic pulling flows, respectively. These flows are shown in Figure 6. The flow induced by a MT being pulled by cortical force generators—the simplest model of the cortical pulling mechanism—is the same as in Figure 6a but in the opposite direction, and thus is not presented here.

General physical principles underlie the gross cytoplasmic flow structures that we observe for the different models. In both cortically based models, the MTs are pushing or being pulled against a fixed boundary (cell periphery) while an opposite force is applied from the cell boundary or the cortically bound dynein motors to the MTs. In such a case, because the force on the outer boundary does not generate any internal flows, the cytoplasmic flows are associated with the motion of the MT under an external force within the cellular confinement. In the case of the cortical pushing mechanism, because the MT plus end is fixed at the cortex, the polymerization forces push the MT away from the cortex to open space for adding

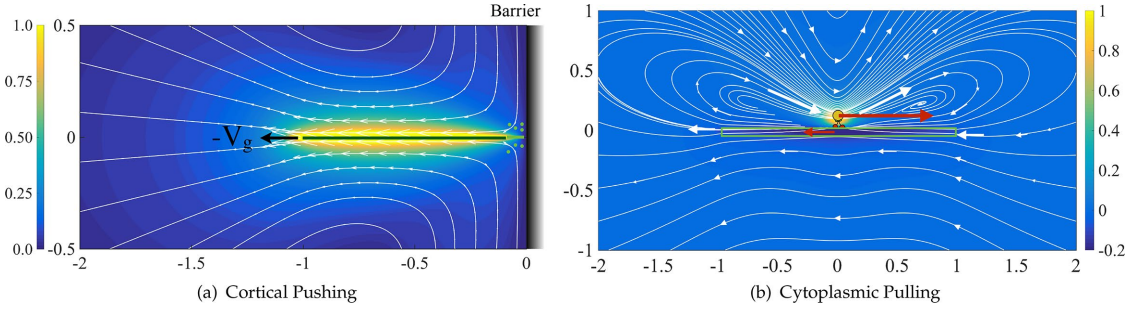

FIGURE 6: (a) Flow induced by MT growing against a barrier and (b) flow induced by a cargo-carrying dynein walking on a MT as simple representations of the cortical pushing and cytoplasmic pulling mechanisms. The induced flows are all three dimensional and are presented only in the plane of the MT and the direction of its motion for visualization. The solid curved lines are the flow streamlines. The arrows tangent to the streamlines are the velocity vectors. The size of the arrows and the background contour plot correspond to the magnitude of fluid velocity. The vectors with only an arrowhead in b correspond to nearly zero fluid velocity, as evident from the contour plot. The maximum and minimum in the color bar in b correspond to the velocity of the cargo and the MT in the *x*-direction, respectively.

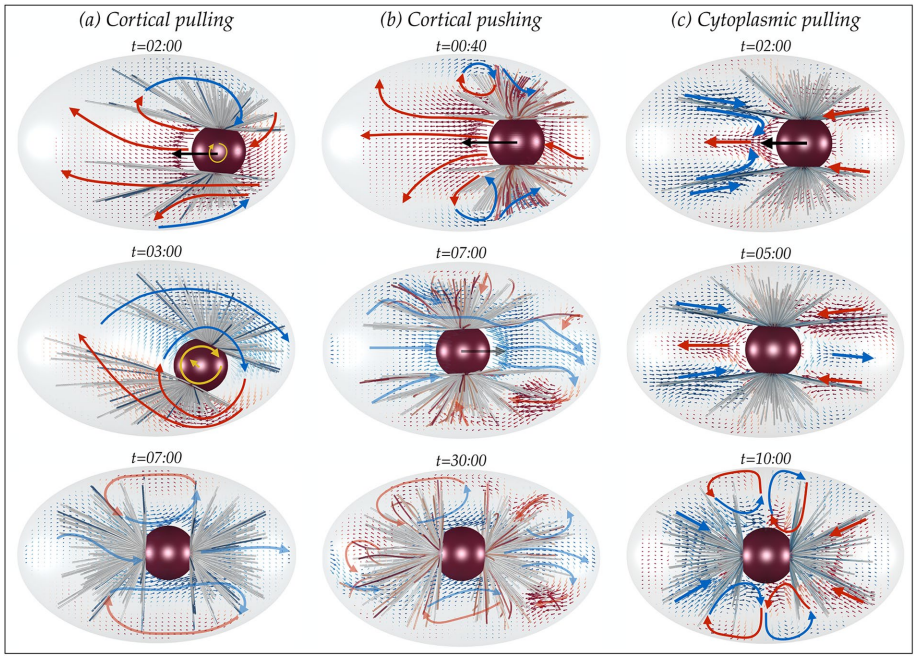

FIGURE 7: Snapshots of cytoplasmic flows at different stages of pronuclear migration: the (a) cortical pulling, (b) cortical pushing, and (c) cytoplasmic pulling mechanisms. Numbers denote time in minutes:seconds after the nuclei meeting. The results are projected onto the *xy*-plane to aid visualization, where the AP axis is the *x*-axis and the intercentrosomal axis is initially aligned with the *y*-axis. Note that both the shape of the MTs and the flow are defined in three dimensions. The faint colors of the velocity vectors in the bottom panel of the cortical pulling flows and the middle and bottom panels of the cortical pushing flows represent the "weakness" of the cytoplasmic flows in those instances compared to the flow strength at the initial stages of the PNC migration. In contrast, the flows in the cytoplasmic pulling model remain "strong" throughout the entire migration process.

the newly formed microtubule materials. This outward flux creates a flow by dragging cytoplasm from the cell periphery into the cell volume (Figure 6a). In the case of the cortical pulling mechanism, the applied force and the resulting cytoplasmic flows are in the opposite direction.

In the cytoplasmic pulling model, the pulling force applied on the MTs by a dynein motor is balanced by the equal and opposite force applied by that motor's cargo onto the cytoplasm through which it is being dragged. Unlike the cortical models, in which the applied forces at the cell boundary do not induce internal flows, the force applied by the dynein motors to the cargo generates a flow in the opposite direction of the MT motion. The flow is then a combination of the flow induced by the motion of the MT and the flow induced by the cargo transport. Because equal and opposite forces are applied to the cargo and the MT, the flow roughly corresponds to the flow induced by a force dipole (Happel and Brenner, 1965). Figure 6b shows the 3D velocity streamlines and spatial variations of velocity magnitude induced by a single dynein motor carrying a 0.1-μm spherical cargo along a 2-μm-long microtubule. The results are projected to the plane of motion of the MT. Note that the flow strength in this model decays much faster than the flow induced by growing/shrinking MTs against barriers and becomes negligible at distances less than the length of the MT.

With these simple examples in hand, we now discuss the computed cytoplasmic flows during pronuclear migration in complete instantiations of the three mechanisms. We start with the cortical pulling mechanism. Because the MTs are hardly deformed in this model, the motion of the entire PNC/MT-array complex generates cytoplasmic flows similar to that of a porous body towed through a confined space. Figure 7a, top, shows a snapshot of the cytoplasmic velocity field at early times, which, at this instant, is dominated by translation and bears a striking resemblance to that shown in Figure 3a, where the PNC/MT array is translated by an external force. At an intermediate time, the cytoplasmic flow has become primarily rotational (Figure 7a, middle). In these conditions, the flow begins to resemble that seen in Figure 3c, where the centered PNC/MT array is rotated by an external torque. At late times (e.g., Figure 7a, bottom), the cytoplasmic flows are weak and arise from fluctuations in PNC position due to the stochastic attachment and detachment of MTs from the cortex. As the MTs remain straight under their extensive loading from cortical force generators, the cytoplasmic velocity fields arise almost entirely from the translations and rotations of the PNC/MT array complex.

For the cortical pushing model shown in Figure 7b, the cytoplasmic flow is a combination of the flows generated by the motion of the PNC/MT-array complex (similar to the flow shown in Figure 3a) and flows due to MT deformations near the periphery. After the MTs reach the cortex and continue polymerizing, they are pushed away from the boundaries with the same speed as they grow. Thus the generated flows near the cortex scale with the plus-end polymerization rate and are primarily in the direction opposite the polymerization direction (Figure 6a). (The generated flows near the cortex can be quite involved: the growth of the buckling amplitude, which is orthogonal to the direction of MTs, also contributes to the flow, as does the relaxation of the MTs switching to catastrophe.) For the range of biophysical parameters used in our simulations, see Table 2. The flow induced by MT deformation near the periphery is comparable in magnitude to that induced by the PNC motion for most of the migration process. Figure 7b, middle and bottom, shows that the same flow patterns are also observed near the periphery after completion of PNC centering and rotation.

Finally, we discuss the flows in the cytoplasmic pulling mechanism. Unlike the cortical pushing and pulling models, which use the cell periphery as the mechanical substrate against which to exert forces through MTs, the force substrate is now the cytoplasm in which the cargoes are immersed. Hence the generated flow arises from two sources: 1) the flow induced by the motion of the PNC/MT-array, and 2) the flow generated by the motion of cargoes toward the minus ends of MTs. Figure 7c shows that the cytoplasmic flows thus produced are fundamentally different than those observed in the two previous models. The key flow signature that is present in all stages of migration is that, unlike the cortical pushing and pulling mechanisms, the cytoplasmic flow in the anterior is in the opposite direction of the motion of the PNC and is along the direction of cargo transport toward the centrosomes in the volume occupied by the astral MTs. The strength of the flow in the cytoplasmic pulling model is determined by the

total active force applied by the dynein motors, which in our model scales with the total length of the MTs. Consequently the strength of flow throughout and after the migration process does not change significantly. On the other hand, the velocity of the PNC monotonically decreases as it approaches the center of the cell. Hence, as we see in Figure 7c, middle and bottom, after centering, the strength of cytoplasmic flows is much stronger than the small fluctuating velocity of the PNC. This leads us to another key difference between the cytoplasmic pulling and cortically based models: in the cytoplasmic pulling model, the fluid velocity magnitude is much larger than that of velocity fluctuations of the PNC after centering, whereas for the other mechanisms, the fluid velocity is similar in magnitude to that of the PNC velocity fluctuations.

The flows arising from cytoplasmic pulling resemble those generated by "puller" microswimmers (Saintillan and Shelley, 2013) such as *Chlamydomonas reinhardtii* (Drescher *et al.*, 2010). The reason lies in the ensemble behavior of the PNC/MT array and the immersed dynein motors. As shown in Figure 7a, for any force applied by the attached dynein motors on the MTs, there is an equal and opposite force applied by the cargoes to the cytoplasmic fluid. Thus, whereas the force on the PNC/MT array is not zero, the net force on the PNC/MT array and the cytoplasmic fluid is identically zero. In particular, the motion of each cargo on the MT array generates a force dipole described by a tensor whose symmetric part gives the net stress on the system, which, unlike the net force, is not zero. For straight MTs and a uniform distribution of the motors, the net stress tensor induced by motor activity is

$$\sigma_{\text{motor}} = \frac{1}{2}\sum_{i=1}^{N} L_i \left(p_i r_i + r_i p_i\right) f_{\text{motor}} \qquad (2)$$

where L_i and p_i are the length and unit tangent vector of the ith MT, respectively, and r_i, taken as orthogonal to p_i, gives the relative position of the cargo with respect to its attachment point on the ith MT. The antisymmetric part of the force dipole determines the net torque on the system, which is also zero. Zero net force and torque and a finite *active* stress are the two hallmarks of active, self-propelled particles (Saintillan and Shelley, 2013). As a result, the flow far from such particles is that generated by the symmetric part of a force dipole. Whereas in our system the size of the "active particle" —the PNC/MT-array—is similar to the scale of its confinement, the flow still closely resembles that generated by a puller particle in an open flow (see Figure 5 of Saintillan and Shelley, 2013).

The cortically based models both generate grossly similar cytoplasmic flows (albeit different MT deformations) because they share the feature that the force is transduced to the PNC by MT pushing/pulling on/from an immobile cell boundary. In these conditions, the net force on the PNC/MT arrays and the cytoplasm is nonzero. The cytoplasmic flows then resemble those generated by a force monopole, or a *Stokeslet*, within a confinement.

DISCUSSION

The motion of cytoskeletal components and payloads within the cytoplasm can generate global flows and long-range HIs between them. Most previous studies related to the mechanics of cytoskeleton ignore the effect of HIs; see Shinar *et al.* (2011) for an exception. In this study, we used detailed dynamic simulations that explicitly account for many-body HIs to demonstrate several important consequences of HIs in the mechanics of the pronuclear migration stage of the first cell division in *C. elegans* embryo. Nevertheless, the findings of this study are quite generic and extendable to other cytoskeletal assemblies.

First, through direct simulation, we showed that the most fundamental effect of HIs in pronuclear migration is that the astral MTs array behaves effectively as a porous medium; see Nazockdast *et al.* (2017) for a more quantitative study. Increasing the number of astral MTs reduces the permeability of the fluid, resulting in larger hydrodynamic dimensions of the PNC and a larger net force/torque associated with moving the PNC to the proper position/orientation. We showed that previous approximations of the PNC drag coefficient, which either ignore HIs or include them partially, overpredict or underpredict active forces by a large factor. By comparing the translational and rotational motion of the PNC and its astral MTs, we showed that the effect of astral MTs cannot be simply reduced to an effective viscosity. This observation has important consequences that go beyond the pronuclear migration problem. For example, consider measuring the effective viscosity of the cell's interior using active microrheology, in which a probe is externally driven through the cytoplasm using magnetic forces and/or optical tweezers with a given force or torque (Wirtz, 2009). The measured translational or angular velocity of the probe is then used to compute the effective viscosity. For a spherical probe, the viscosity is computed using $\mu = F/(6\pi U a)$ or $\mu = F/(6\pi\Omega a^3)$ for cases of applying a fixed external force F or torque L, respectively. If the cellular interior acts as a porous medium—because the hydrodynamic effect of the astral MTs cannot be modeled with an effective viscosity—the computed viscosities from these two models (applying a force vs. a torque) may yield viscosities that differ considerably. Instead, if the astral MTs were not attached to the PNC and were freely suspended in the cytoplasm, these two experiments would be expected to give similar results for the viscosity.

We studied the dynamics of PNC/MT-array positioning using simple instantiations of the cortical pulling, cortical pushing, and cytoplasmic pulling mechanisms. Our results show that all three mechanisms can center and rotate the PNC within reasonable times and range of biophysical parameters. Thus proper positioning alone cannot identify the main mechanism of PNC migration. We propose that the structure of cytoplasmic flows may select between the different possible active mechanisms involved in cellular processes such as pronuclear migration. We show, through simulation, that each of these force transduction mechanisms leaves its specific fingerprint in the generated cytoplasmic flows; these features are directly related to how the force is transferred from molecular motors and cell boundaries to the MTs. Specifically, we show that when the active forces are applied from an immobile substrate to the MTs, such as in the cortical pushing and pulling mechanisms, the basic feature of the cytoplasmic flows is that of the flow generated by a point force (Stokeslet) in a confined geometry. In the cytoplasmic pulling mechanism, in which the substrate is mobile (cargo-carrying dynein), the generated flow is the combination of the flow generated by the average motion of the PNC/astral MT and flow induced by cargo transport, which resembles the flows induced by a force dipole.

These aspects of flow signatures are generic features of each active mechanism and do not depend on details such as the value of the shear viscosity of the cytoplasm, the MT bending rigidity, the stall force of the molecular motors, or their force–velocity relationship. Thus they can be used to study the possible contributions of these differing force transduction mechanisms in other stages of cell division and possibly other cytoskeletal structures. We are following up on these ideas by directly measuring the cytoplasmic flows by particle-tracking methods.

ACKNOWLEDGMENTS

We thank Sebastian Füerthauer, Hassan Masoud, Tong Gao, Michael O'Neal, and Carlos Garzon-Coral for helpful discussions. We acknowledge support from National Institutes of Health Grant 1R01GM104976-01. E.N. and M.S. acknowledge support from National Institutes of Health Grant 1R01GM104976-01 and National Science Foundation Grants DMS 1463962 and DMS-1620331. A.R. acknowledges the support of the National Science Foundation through Grant DMS-1320621.

REFERENCES

Broedersz CP, Mackintosh FC (2014). Modeling semiflexible polymer networks. Rev Mod Phys 86, 995.

Cowan CR, Hyman AA (2004). Asymmetric cell division in C. elegans: cortical polarity and spindle positioning. Annu Rev Cell Dev Biol 20, 427–453.

Drescher K, Goldstein RE, Michel N, Polin M, Tuval I (2010). Direct measurement of the flow field around swimming microorganisms. Phys Rev Lett 105, 168101.

Garzon-Coral C, Fantana HA, Howard J (2016). A force-generating machinery maintains the spindle at the cell center during mitosis. Science 352, 1124–1127.

Goulding MB, Canman JC, Senning EN, Marcus AH, Bowerman B (2007). Control of nuclear centration in the C. elegans zygote by receptor-independent Gα; signaling and myosin II. J Cell Biol 178, 1177–1191.

Grill SW, Gönczy P, Stelzer EH, Hyman AA (2001). Polarity controls forces governing asymmetric spindle positioning in the Caenorhabditis elegans embryo. Nature 409, 630–633.

Hamaguchi MS, Hiramoto Y (1986). Analysis of the role of astral rays in pronuclear migration in sand dollar eggs by the colcemid-uv method. Dev Growth Differ 28, 143–156.

Happel J, Brenner H (1965). Low Reynolds Number Hydrodynamics, Leiden, Netherlands: Martinus Nijhoff.

Holy TE, Dogterom M, Yurke B, Leibler S (1997). Assembly and positioning of micro- tubule asters in microfabricated chambers. Proc Natl Acad Sci USA 94, 6228–6231.

Howard J (2001). Mechanics of Motor Proteins and the Cytoskeleton, Sunderland, MA: Sinauer.

Kimura A, Onami S (2005). Computer simulations and image processing reveal length-dependent pulling force as the primary mechanism for C. elegans male pronuclear migration. Dev Cell 8, 765–775.

Kimura A, Onami S (2007). Local cortical pulling-force repression switches centrosomal centration and posterior displacement in C. elegans. J Cell Biol 179, 1347–1354.

Kimura K, Kimura A (2011). Intracellular organelles mediate cytoplasmic pulling force for centrosome centration in the Caenorhabditis elegans early embryo. Proc Natl Acad Sci USA 108, 137–142.

Labbé JC, Mccarthy EK, Goldstein B (2004). The forces that position a mitotic spindle asymmetrically are tethered until after the time of spindle assembly. J Cell Biol 167, 245–256.

Longoria RA, Shubeita GT (2013). Cargo transport by cytoplasmic dynein can center embryonic centrosomes. PLoS One 8, e67710.

McNally FJ (2013). Mechanisms of spindle positioning. J Cell Biol 200, 131–140.

Nazockdast E, Rahimian A, Zorin D, Shelley MJ (2017). A fast platform for simulating semi-flexible fiber suspensions applied to cell mechanics. J Comput Phys 329, 173–209.

Nedelec F, Foethke D (2007). Collective Langevin dynamics of flexible cytoskeletal fibers. New J Phys 9, 0–24.

Payne C, Rawe V, Ramalho-Santos J, Simerly C, Schatten G (2003). Preferentially localized dynein and perinuclear dynactin associate with nuclear pore complex proteins to mediate genomic union during mammalian fertilization. J Cell Sci 116, 4727–4738.

Reinsch S, Gönczy P (1998). Mechanisms of nuclear positioning. J Cell Sci 111, 2283–2295.

Saintillan D, Shelley M (2013). Active suspensions and their nonlinear models. CR Phys 14, 497–517.

Shelley MJ (2016). The dynamics of microtubule/motor-protein assemblies in biology and physics. Annu Rev Fluid Mech 48, 487–506.

Shinar T, Mana M, Piano F, Shelley MJ (2011). A model of cytoplasmically driven microtubule-based motion in the single-celled Caenorhabditis elegans embryo. Proc Natl Acad Sci USA 108, 10508–10513.

Siller KH, Doe CQ (2009). Spindle orientation during asymmetric cell division. Nat Cell Biol 11, 365–374.

Tornberg A-K, Shelley MJ (2004). Simulating the dynamics and interactions of flexible fibers in Stokes flows. J Comput Phys 196, 8–40.

Tran PT, Marsh L, Doye V, Inoue S, Chang F (2001). A mechanism for nuclear positioning in fission yeast based on microtubule pushing. J Cell Biol 153, 397–412.

Tsou M-FB, Hayashi A, Debella LR, Mcgrath G, Rose LS (2002). LET-99 determines spindle position and is asymmetrically enriched in response to PAR polarity cues in C. elegans embryos. Development 129, 4469–4481.

Wirtz D (2009). Particle-tracking microrheology of living cells: principles and applications. Annu Rev Biophys 38, 301–326.

Supplemental Materials

Molecular Biology of the Cell

Nazockdast et al.

Supplementary Materials

Ehssan Nazockdast [*1,2], Abtin Rahimian [1], Daniel Needleman [3], and Michael Shelley [1,2]

[1]Simons Foundation, Flatiron Institute, Center for Computational Biology, 162 fifth Avenue, New York, NY 10010
[2]Courant Institute of Mathematical Sciences, New York University, 251 Mercer Street, New York, NY 10012
[3]School of Engineering and Applied Sciences, Harvard University, 29 Oxford Street Cambridge, MA 02138

February 22, 2017

1 Numerical methods

In this section we give a brief description of the highly efficient computational method used to simulate the hydrodynamic interactions (through the cytoplasm) of MTs with each other, the pronuclear complex, and the cell cortex. This method also accounts stably for MT flexibility, their dynamic instability, and their interactions with molecular motors. Further details of the numerical method is given in [Nazockdast *et al.*, 2017]. For cellular flows inertial effects can be safely ignored. While we assume the cytoplasm is assumed Newtonian [Daniels *et al.*, 2006], the mechanical responses of the overall system of cytoplasm and cytoskeleton is in general non-Newtonian. The flow of a Newtonian cytoplasm is described by the incompressible Stokes equation:

$$\mu\Delta\boldsymbol{u} - \nabla p = \mathbf{0} \;\;\&\;\; \nabla\cdot\boldsymbol{u} = 0, \tag{1}$$

where μ is the bulk viscosity, $\boldsymbol{u}$ is the (cytoplasmic) fluid velocity, and p is the pressure. We represent solutions to the Stokes equations using a boundary integral formulation [Pozrikidis, 1992], where the fluid velocity is represented as a distribution of fundamental solutions to the Stokes equations on all immersed and bounding surfaces. The densities of these distributions is determined by the application of boundary conditions, such as the no-slip condition (surface velocity is equal to fluid velocity). A boundary integral formulation reduces the computational problem from 3D (solving the Stokes equations in the fluid volume) to the 2D problem of solving coupled singular integral equations on all the immersed and bounding surfaces. In formulating the contributions from the bounding surface S_E (the cortex) and any surfaces of internal bodies S_I (here, only the PNC), we use a distribution of stresslets, a representation due to [Power & Miranda, 1987] which generates well-conditioned 2^{nd}-kind Fredholm integral equations. The contributions due to the motion of MTs are be treated specially due to their slenderness, as their surface integrals can be reduced, through asymptotics, to integrals of Stokeslets along their center-lines.

To be specific, consider N MTs attached to the pronuclear complex, with the entire structure contained within the cell cortex. The n^{th} MT has center-line position $\boldsymbol{X}_n(s,t)$, where s is arclength measured from the

*ehssan@cims.nyu.edu

point of attachment and $0 \leq s \leq L_n$ with L_n the MT's length. Then, the fluid velocity at a point $\mathbf{x}$ within the cytoplasm can be given as

$$\mathbf{u}(\mathbf{x}) = \mathbf{u}_{MT}(\mathbf{x}) + \mathbf{u}_E(\mathbf{x}) + \mathbf{u}_I(\mathbf{x}) \quad \text{where} \tag{2a}$$

$$\mathbf{u}_{MT}(\mathbf{x}) = \sum_{m=1}^{N} \mathbf{u}_{MT,m}(\mathbf{x}) = \sum_{m=1}^{N} \int_0^{L_m} \boldsymbol{G}(\mathbf{x} - \boldsymbol{X}_m(s')) \cdot \boldsymbol{f}_m(s') ds' \tag{2b}$$

$$\mathbf{u}_E(\mathbf{x}) = \int_{S_E} \boldsymbol{q}_E(\mathbf{x}') \cdot \boldsymbol{T}(\mathbf{x} - \mathbf{x}') \cdot \boldsymbol{n}(\mathbf{x}') dS_{x'} \tag{2c}$$

$$\mathbf{u}_I(\mathbf{x}) = \int_{S_I} \boldsymbol{q}_I(\mathbf{x}') \cdot \boldsymbol{T}(\mathbf{x} - \mathbf{x}') \cdot \boldsymbol{n}(\mathbf{x}') dS_{x'} + \boldsymbol{G}(\mathbf{x} - \mathbf{x}_c) \cdot \boldsymbol{F}_I^{ext} + \boldsymbol{R}(\mathbf{x} - \mathbf{x}_c) \cdot \boldsymbol{L}_I^{ext} \tag{2d}$$

That is, the velocity is expressed as a sum of three sets of integrals, over MTs centerlines, the external boundary (S_E; the cortex), and internal boundaries (S_I; the pronuclear complex). Here $\boldsymbol{G}(\boldsymbol{r}) = (\boldsymbol{I} + \hat{\boldsymbol{r}}\hat{\boldsymbol{r}})/(8\pi\mu|\boldsymbol{r}|)$, with $\hat{\boldsymbol{r}} = \boldsymbol{r}/|\boldsymbol{r}|$, is the single-layer fundamental solution for the Stokes equations (the Stokeslet, a 2^{nd} rank tensor), μ is the fluid viscosity, and $\mathbf{f}_m$ is the force/length that the m^{th} MT exerts upon the fluid; $\boldsymbol{T} = -3\hat{\boldsymbol{r}}\hat{\boldsymbol{r}}\hat{\boldsymbol{r}}/(4\pi\mu|\boldsymbol{r}|^2)$ is the double-layer fundamental solution (the stresslet, a 3^{rd} rank tensor), and $\boldsymbol{q}_{E,I}$ are vector densities to be determined [Power & Miranda, 1987]. Note that a distribution of stresslets on the surface of a body (immersed in a Stokesian fluid) produces identically zero net force and/or torque upon that body. Thus, in Eq. (2c), to account correctly for any applied forces and torques, explicit Stokeslet and Rotlet singularities are included inside the body. In particular, $\boldsymbol{F}^{ext}$ and $\boldsymbol{L}^{ext}$ are the external force and torque, respectively, exerted upon the PNC (S_I) where $\boldsymbol{R}(\boldsymbol{r}) \cdot \boldsymbol{L} = \boldsymbol{L} \times \hat{\boldsymbol{r}}/(8\pi\mu|\boldsymbol{r}|^2)$ is the *Rotlet* fundamental solution to the Stokes equations, and $\mathbf{x}_c$ is any point interior to S_I. Finally, the vector $\boldsymbol{n}$ is the unit outer normal to the S_E and S_I surfaces.

Taking the two limits $\mathbf{x} \to S_I$ or S_E generates integral equations for the densities $\boldsymbol{q}_{E \text{or} I}$, respectively. Requiring that the outer boundary S_E be stationary, or $\mathbf{u}(\mathbf{x}) = \mathbf{0}$ for $\mathbf{x} \in S_E$, generates the limiting integral equation

$$\mathbf{u}_{MT}(\mathbf{x}) + \mathbf{u}_I(\mathbf{x}) - 4\pi\boldsymbol{q}_E(\mathbf{x}) + \int_E \boldsymbol{q}_E(\mathbf{x}') \cdot \boldsymbol{T}(\mathbf{x}' - \mathbf{x}) \cdot \hat{\boldsymbol{n}}(\mathbf{x}') dS_{x'} = \mathbf{0}, \tag{3}$$

Likewise, the limiting integral equation for $\mathbf{x} \in S_I$ is

$$\begin{aligned} &\mathbf{u}_{MT}(\mathbf{x}) + \mathbf{u}_E(\mathbf{x}) + 4\pi\boldsymbol{q}_I(\mathbf{x}) \\ &\quad + \int_I \boldsymbol{q}_I(\mathbf{x}) \cdot \boldsymbol{T}(\mathbf{x}' - \mathbf{x}) \cdot \hat{\boldsymbol{n}}(\mathbf{x}) dS_{x'} + \boldsymbol{G}(\mathbf{x} - \mathbf{x}_c) \cdot \boldsymbol{F}_I^{ext} + \boldsymbol{R}(\mathbf{x} - \mathbf{x}_c) \cdot \boldsymbol{L}_I^{ext} = \boldsymbol{U}_I \boldsymbol{\Omega}_I \times (\mathbf{x} - \mathbf{x}_c), \end{aligned} \tag{4}$$

where $\boldsymbol{U}$ and $\boldsymbol{\Omega}$ are the translational and angular velocity of the immersed body. In both Eqs. (3) & (4), the singular surface integrals are interpreted in the principal value sense.

One cannot take a limit of Eq. (2b) as $\mathbf{x}$ approaches a point on an MT. The resulting integral is undefined and the problem is instead treated through careful asymptotics [Keller & Rubinow, 1976; Johnson, 1980; Götz, 2000]. In this case it has been established that the velocity of the n^{th} MT center-line, $\boldsymbol{U}_n = \partial \boldsymbol{X}_n / \partial t$, is given to leading order by

$$\boldsymbol{U}_n = \sum_{m=1}^{N} \mathbf{u}_{MT,m \neq n}(\boldsymbol{X}_n) + \mathbf{u}_E(\boldsymbol{X}_n) + \mathbf{u}_I(\boldsymbol{X}_n) + (\ln(\epsilon^{-2}e^{-1})/8\pi\mu)\,(\boldsymbol{I} + \boldsymbol{X}_{n,s}\boldsymbol{X}_{n,s}) \cdot \boldsymbol{f}_n(s), \tag{5}$$

where we have assumed that arclength parameter is also a material parameter of the MT fiber which is a consequence of MT inextensibility. The subscript s on $\boldsymbol{X}_{n,s}$ denotes a partial derivative with respect to s (hence, $\boldsymbol{X}_{n,s}$ is the MT tangent vector), and $\epsilon = a/L_n$ is the MT aspect ratio. Here, we have neglected the velocity contribution from nonlocal self interactions of different segments of each individual fibers, which arise as a result of having curvature and non-uniform distribution of forces along the fiber. This interaction

contributes to the velocity of the fiber to $\mathcal{O}(1)$ compared with the leading $\ln(\epsilon^{-2}e^{-1})$ term. Our numerical experiments [Nazockdast *et al.*, 2017] show that including these nonlocal self interactions has negligible effect on the overall dynamics.

The force applied from an MT to the fluid, $\boldsymbol{f}$, is balanced with the hydrodynamic force from the fluid to the MT and is the sum of internal elastic forces and the forces applied by molecular motors or through interactions with the boundaries. External forces can be applied either at the MT ends (through boundary conditions), or along the length of the MT where $\mathbf{f} = \mathbf{f}^{\text{elastic}} + \mathbf{f}^{\text{motor}}$. The elastic forces are related to MT conformation through Euler-Bernouli beam theory by the constitutive relation $\boldsymbol{f}^{elastic} = -E\boldsymbol{X}_{ssss} + (T\boldsymbol{X}_s)_s$, with E the MT flexural modulus, and T is the MT's axial tension. The term $-E\boldsymbol{X}_{ssss}$ is the bending force per unit length and $(T\mathbf{x}_s)_s$ is tension force per unit length. The tension T is determined by the condition of MT inextensibility [Tornberg & Shelley, 2004]. This constraint gives an auxiliary equation for tension by imposing $\boldsymbol{U}_s \cdot \boldsymbol{X}_s = 0$ which follows from differentiating the identity $\boldsymbol{X}_s \cdot \boldsymbol{X}_s = 1$ and interchanging s and t derivatives; that these derivatives can be interchanged follows from assuming s gives a material parametrization of the MT position.

One method for modeling the (de)polymerization process is to discretely remove/add finite length segments from/to MTs in time. Our numerical experiments based on this approach shows that, to avoid numerical instabilities, extremely small time steps are needed. To overcome this limitation, we instead introduce a new parameterization variable, α, of the MT centerline satisfying $\alpha = s/L(t)$ so that $0 \leq \alpha \leq 1$, and L then appears explicitly in the reformulated equations. This removes the numerical instability and allows us to take much larger time-steps, now dictated by considerations of accuracy rather than numerical stability.

To fully determine the dynamics of the MTs and the PNC requires specifying $\boldsymbol{f}^{\text{motor}}$ which depends on the particular model of motor-protein type and activity. Three different models of PNC migration, resulting in different forms for $\boldsymbol{f}^{\text{motor}}$ are discussed in the next sections. Once $\boldsymbol{f}^{\text{motor}}$ is specified, Eqs. (4)-(5) are discretized using pseudo-spectral methods in space and an explicit/implicit backward time-stepping scheme. The latter treats the bending forces and tension implicitly (among other elements), which removes the high-order stability stiffness constraints from elasticity, so that the time-step is chosen by the requirements of accuracy rather than numerical stability Nazockdast *et al.* [2017]. This results in a linear system of equations to be solved at each time-step. For this, we use GMRES [Saad & Schultz, 1986] with special purpose preconditioners [Nazockdast *et al.*, 2017]. If each fiber is discretized by M points, direct computation of the HIs between the N MTs requires $(N \times M)^2$ operations which is very demanding for $\mathcal{O}(1000)$ or more MTs. We instead use a *Kernel-Independent* [Ying *et al.*, 2004] implementation of the Fast Multipole Method (FMM) [Greengard & Rokhlin, 1987] to speed up the computation HIs, reducing the cost to $\mathcal{O}(N \times M)$. All the computations, including the FMM, are parallelized and scaleable.

2 Biophysical models for positioning and their properties

2.1 Cortical pushing

In the *cortical pushing* model, positioning is achieved by repulsive forces applied from the cortex when a growing MT reaches the cell boundary. The magnitude of the force is such that it stops the growth reaction process, or provides space for growth through moving the PNC away from the cortex or by deforming the growing fiber. *In vitro* measurements suggest that the stall force for growth process of the MTs is $F_P^S \approx 4.4$ pN [van Doorn *et al.*, 2000]. If we take the average length of the astral MTs reaching the cortex throughout the centering process to be approximately $15\,\mu$m –assuming that the MTs rarely go through catastrophe prior to reaching the cell cortex– the force threshold for a bucking instability is $F^B = \pi^2 E/L^2 \approx 0.4\,\text{pN} \ll 4.4\,\text{pN}$. Thus, in most interactions of MTs with cortex, MTs bend or buckle and continue the growth process rather than completely stalling it. Hence, larger forces are applied to the side of PNC with shorter MTs (larger buckling forces) resulting in the centering of the PNC.

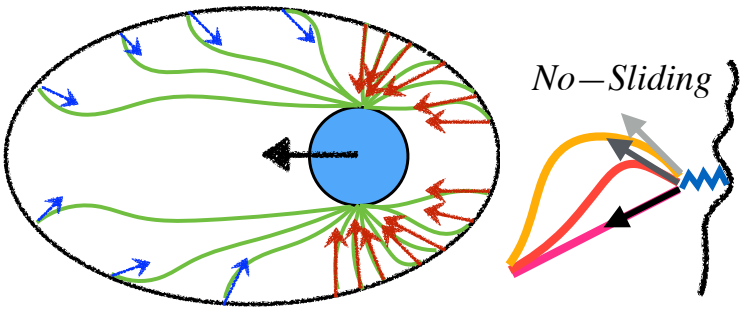

Figure 1: *A schematic of the no-sliding cortical pushing model, where the plus end of the growing MTs remain attached to the cortex with a spring force.*

We consider two variations of this model namely the *free-sliding* and *no-sliding* sub-models. The main text only focuses on the predictions of the no-sliding model, as only this model gives proper alignment of the centrosomal axis with AP axis. The free-sliding model and its predictions are described only in the Supplementary Materials and in section §3.

In the *no-sliding* model, we constrain the sliding and growth along the boundaries and assume that the growing plus-ends of MTs remain fixed on the cortex as long as they are growing. We implement this constraint by a linear spring force at the attachment point: $\boldsymbol{F}^M = -K\,(\boldsymbol{X} - \boldsymbol{X}_{\text{att}})$, where K is the spring constant (set to 10 pNμm^{-1}), and where $\boldsymbol{X}_{\text{att}}$ is the pinned plus-end position of the MT set by having reached a distance closer than $\Delta r^\star = 0.5\ \mu$m to the cortex. This is shown schematically in Fig. 1. At 0.5 μm of displacement, this choice of K results in 5 pN of force, which is bigger than the stall force for polymerization reaction ($F_S^P = 4.4$ pN). Thus, the MTs will stop growing prior to reaching to the cell periphery. In both variations of the model, we use the empirical model given by Dogterom & Yurke [1997] based on their *in vitro* experimental studies, and relate the rate of growth to the applied end-force by $V_g = A\exp\left(-C(F^M\cdot\boldsymbol{x}_s)/F_P^S\right) - B$ with $A = 1.13\,\mu\text{m}\,\text{min}^{-1}$, $B = -0.08\,\mu\text{m}\,\text{min}^{-1}$, and $C = 2.33$.

The *in vitro* measurements of Janson *et al.* [2003] suggest that the turnover time of MTs in contact with cortex is proportional to their growth velocity. The measured rates of catastrophe in [Janson *et al.*, 2003] are however generally smaller than 0.1 s^{-1} while *in vivo* observations suggest 0.5-1 s^{-1} [McNally, 2013]. We use these observations and set the catastrophe rate to

$$f_{\text{cat}} = \max(f_{\text{cat}}^0 \frac{V_g^0}{V_g}, f_{\text{min}}) \tag{6}$$

where f_{cat}^0 is the rate of catastrophe under no compressive load. We include f_{min} as the minimum allowed average rate of catastrophe in the model to incorporate the *in vivo* observations. We have changed this value from 0.1-0.33 s^{-1} to study its effect on the dynamics of migration, with the results presented in section §5. Finally, variations of $\Delta r^\star$ in the free-sliding model and spring stiffness, K, in the no-sliding model did not change the time-scales of PNC migration.

2.2 Cortical Pulling

Our model for cortical pulling on the PNC is based on the asymmetric attachment of MTs to cortically bound dyneins on the anterior and posterior sides of the cell. It closely follows the model prosed by Kimura & Onami [2007], and is motivated by experiments of Tsou *et al.* [2002] showing that LET-99 protein is highly enriched on the posterior side of the cortex in regions close to the mid-plane. LET-99 prevents MTs from attaching to cortically bound dyneins, and results in asymmetric pulling forces and a net force on the PNC towards the anterior. Following Kimura & Onami [2007], we assume that the rate of MT capture

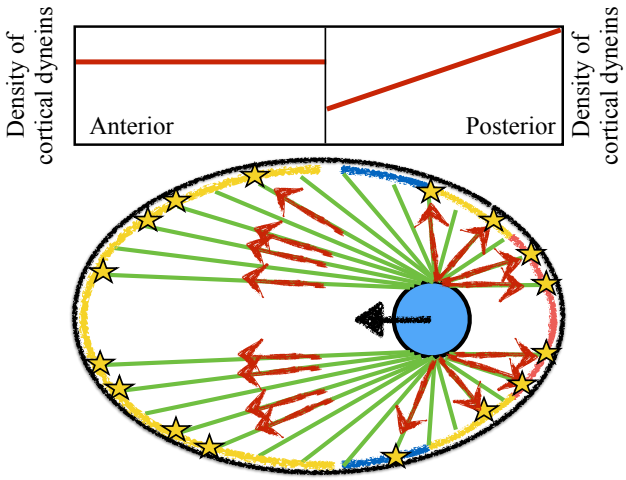

Figure 2: *A schematic of the cortical pulling model model; the stars represent the active cortical dyneins pulling on the MTs. The activated dyneins are uniformly distributed on the anterior side while on the posterior side their density decreases linearly with distance from the pole the to the mid-plane. The blue, yellow and red colors on the boundaries denote, low, average and high number, respectively, of attached MTs.*

by cortically bound dyneins on the anterior cortex is constant, while the capture rate on the posterior side decreases linearly with distance along the AP axis from the posterior pole to the PNC center; see Fig. 2. Also, following Kimura & Onami [2007] and the experimental findings of Grill *et al.* [2003], we take the maximum rate of attachment on the posterior side to be $3/2$ times larger than on the anterior. The slope of decrease in attachment probability is determined by imposing force balance at the PNC center.

In our model, the number of motors on the cortex is finite. For the simulation results presented in the main text, this number is 100. Each motor applies 3 pN force along the captured MTs plus-end tangent direction ($\boldsymbol{F} = 3\boldsymbol{X}_s|_{s=L}$) [Gönczy *et al.*, 1999; Howard, 2001]. We assume that the motors are distributed uniformly on the surface of the cortex, and the asymmetric activation of the motors is implemented by taking the probability of attachment of MTs to cortically bound dyneins a linearly decaying function of the distance from the posterior pole on the posterior side of the cell, while on the anterior side the probability is taken to be uniform. Also each motor can only attach to a single MT. Finally the detachment rate of the cortically attached MTs is assumed constant ($0.3\,\mathrm{min}^{-1}$). These chosen parameters for the number of motors, the end-forces from individual cortically bound dynein, and the detachment rate of the captured MTs are in general agreement with the estimates from [Redemann *et al.*, 2010] who used softened cell membranes to estimate the number of cortical force generators at the end of anaphase.

2.3 Cytoplasmic pulling

In the cytoplasmic pulling model, cargo-carrying dyneins walk towards the minus-ends of MTs and apply a pulling force on MTs that is equal and opposite to the hydrodynamic force needed to push the cargo through the cytoplasmic fluid. The basics are that a PNC starting migration on the posterior side of the cell has centrosomal MTs that can grow longer in the anterior direction than in the posterior. This leads to more attached cytoplasmic dyneins and payloads and hence a net force on the PNC towards the anterior [Kimura & Onami, 2005, 2007; Kimura & Kimura, 2011; Shinar *et al.*, 2011]. A schematic of this model is presented in Fig. 3. The force that dyneins apply to MTs is related to their walking speed through a force-velocity relationship of a single motor as $F = F^{\mathrm{stall}}\,(1 - \max(|V|, V_{\mathrm{max}})/V_{\mathrm{max}})$ [Shinar *et al.*, 2011], where F^{stall} and V_{max} are the stall force and maximum walking speed of the motor. The force and velocity of the motor

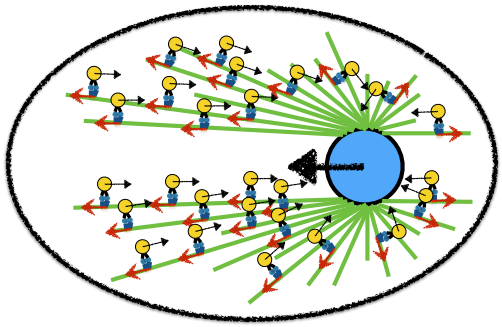

Figure 3: *A schematic of the cytoplasmic pulling model. More cytoplasmic dyneins are attached to the anterior MTs of longer lengths. As a result the PNC moves towards the anterior side until it centers. The cytoplasmic flows arise from the motion of the PNC and the astral MTs, and the motion of cargos towards the centrosomes.*

are also related by the drag coefficient of the cargo: $F = \gamma_{\text{cargo}} V$. Combining the two relationships gives $F^{\text{motor}} = F^{\text{stall}} V_{\text{max}} / \left(V_{\text{max}} + F^{\text{stall}}/\gamma_{\text{cargo}}\right)$. Here we have assumed that the PNC velocity is negligible in comparison to the walking speed of motor-proteins. If we take the cargo to be approximately a sphere with an average radius of $0.25\,\mu$m, we can compute the average force and velocity of the dynein motors that are $F^{\text{motor}} = 0.83F^{\text{stall}} \approx 0.91$pN and $V = 0.2V_{\text{max}} = 0.4\mu\,\text{m s}^{-1}$. Assuming the migration process takes place in roughly 5min, the average velocity of PNC is $V_{\text{PNC}} \approx 0.065\mu\text{m s}^{-1}$, which is much smaller than the walking speed of the motors and does not play a determining role in the analysis given for force-velocity relationship of the motors. We assume a uniform probability of attachment of dynein motors on the MTs and model the force applied by the motors by a continuum model: $\boldsymbol{f}^{\text{motor}} = 0.83 n_{\text{dyn}} F^{\text{stall}} \boldsymbol{X}_s$ where n_{dyn} is the number of the attached dyneins per unit length and is the only fitting parameter in the simulations. The predicted centering and rotation times with the choice of $n_{\text{dyn}} = 0.1\,\mu\text{m}^{-1}$ (presented in this study) was found to be in the range of experimentally observed values that is approximately 5 min.

3 The free-sliding cortical pushing model

In the *free-sliding* model, we assume that the cortical repulsive forces are applied only along the normal direction to the surface i.e. the MTs cannot penetrate the boundary but they can grow or slide freely in the directions tangent to the boundary. We model this using a soft repulsive force,

$$\boldsymbol{F}^M = -F_P^S \exp(-\Delta r/\Delta r^\star)\,(\hat{\boldsymbol{n}}_{cor} \cdot \boldsymbol{x}_s)\,\hat{\boldsymbol{n}}_{cor},$$

where Δr is the minimum distance of the MT plus-end from the cortex. We set $\Delta r^\star = 0.5\ \mu$m, which allows us to simulate the dynamics using reasonable time-steps. When the MTs align tangentially to the boundary, $|\boldsymbol{x}_s \cdot \hat{\boldsymbol{n}}_{\text{cor}}| \ll 1$. This results in vanishing end-point force on them. A schematic of this model is shown in Fig. 4a.

Figure 4c shows a snapshot from long-time simulation of the free-sliding model and points to the key difference between the free-sliding and the no-sliding models: while both models yield centration of the PNC/MT-array complex, only the no-sliding model shows rotation of the intercentrosomal axis to proper position (see also Fig. 4b). Another difference is the conformation of the MTs in these two models. In the free-sliding model the MTs near the cell cortex are *bent* and aligned with the boundary, while, as shown in the main text, the no-sliding model results in the *buckling* of MTs near the boundary.

We now present and discuss the generated flows of the free-sliding model in Fig. 5. Recall that flows in both cortical pushing models are generated by the average motion of the PNC/MT-array complex (similar to the flow shown in Fig. 3a of the main text) and flows due to MT deformations near the periphery

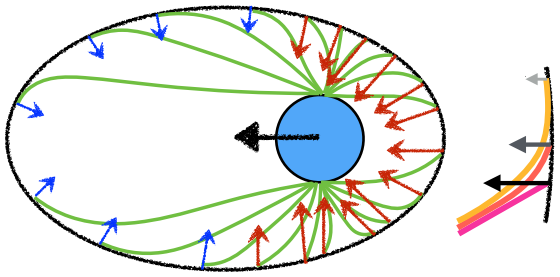

(a) Schematic of the free-sliding model

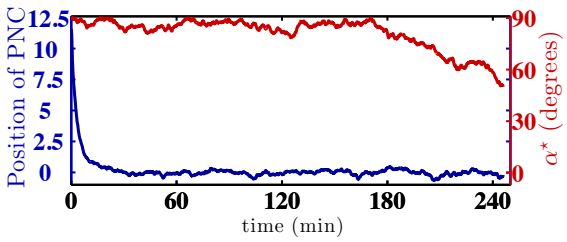

(b) Position & alignment of the PNC

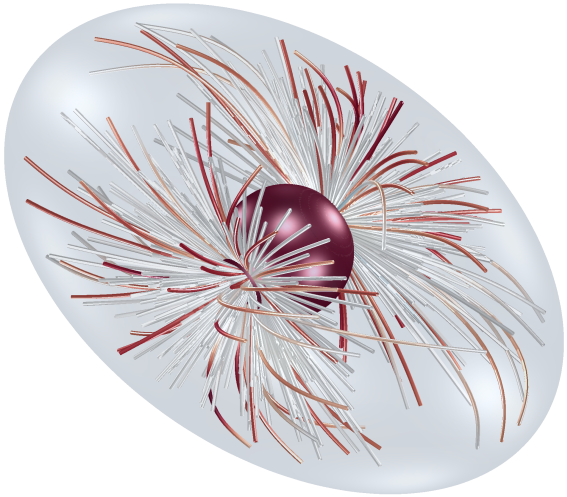

(c) A 3D snapshot of long-time simulations

Figure 4: *(a) A schematic presentation of the cortical pushing free-sliding cortical pushing model. In this case the repulsive force is applied normal to the cortex and the magnitude of the force is re- duces as MTs bend and become more aligned with the cortex. (b) A 3D snapshot of the long-time simulation results. (c) The variations of PNC position and the angle between intercentrosomal axis and AP-axis with time. The PNC properly centers but fails to rotate in a physiologically reasonable time.*

(shown schematically in Fig. 6a of the main text). The difference between the cytoplasmic flows of these two variations of the cortical pushing model arises from the difference in the deformations of their MTs. In the free-sliding model, the end-forces acting on the MTs, as well as the strength of the flow generated by them, decrease as the MTs bend and align further with the cortex. Indeed, in the limit of MTs being aligned with the cortex the growth reaction does not generate any flow, and Fig. 5b and Fig. 5c show that many MTs are aligned with the cortex in this model. As a result, unless the PNC is within 20% of the AP-axis length from the center, the flow induced by the average motion of the PNC/MT-array complex in the free-sliding model has a dominating effect and the flow remains qualitatively similar to that of moving PNC and the attached MTs under an external force shown in Fig. 3a of the main text. However, upon approaching the center the PNC velocity vanishes and the weak flow induced by the deformations of the MTs near the periphery becomes comparable to the weakening flow induced by motion of the PNC/MT-arrays; a snapshot of the flow in this regime is shown in Fig. 5b and Fig. 5c where the arrows show the fluid flow streamlines which are in the direction of bending deformations and orthogonal to the cortex.

4 A torque instability in cortical pushing models

We provide a simplified model to demonstrate the minimum physics required for observing the torque instability that arises in cortical pushing models, which then properly aligns the intercentrosomal axis with the AP-axis. A schematic of the model is given in Fig. 6(a). Here, we assume the PNC is centered and that the intercentrosomal axis forms the angle $\alpha^\star$ with the AP-axis, and N *straight* MTs are interacting with the

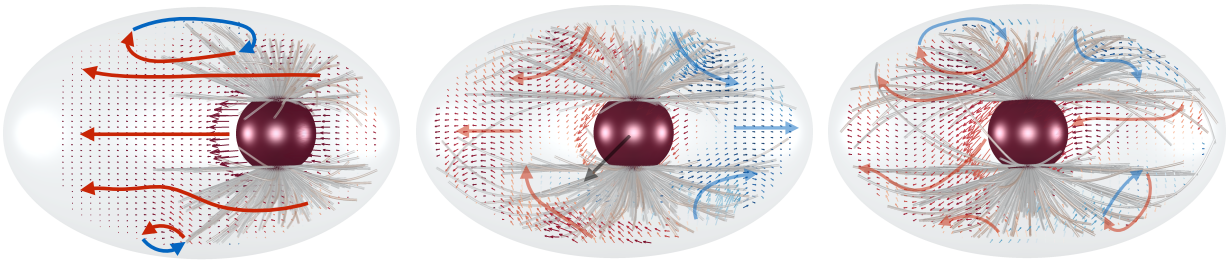

(a) *t=0:40* (b) *t=14:00* (c) *t=180:00*

Figure 5: *Snapshots of the cytoplasmic flows in the free-sliding submodel. These flows arise from the motion of the PNC and the astral MTs, and the deformations of the MTs near the cortex. The cytoplasmic flow prior to centering is dominated by the motion of the PNC and the attached MTs.*

cortex. We consider two models for the pushing force applied from the cortex :

$$\mathbf{F}^1(L) = -\lambda_1 E L^{-2}\hat{\mathbf{n}} \tag{7a}$$

$$\mathbf{F}^2(L) = -\lambda_2 E L^{-2}\hat{\mathbf{p}} \tag{7b}$$

where L is the length of the MT, $\hat{\mathbf{n}}$ is the normal to the surface pointing outwards and $\hat{\mathbf{p}}$ is the unit alignment vector of the MT.

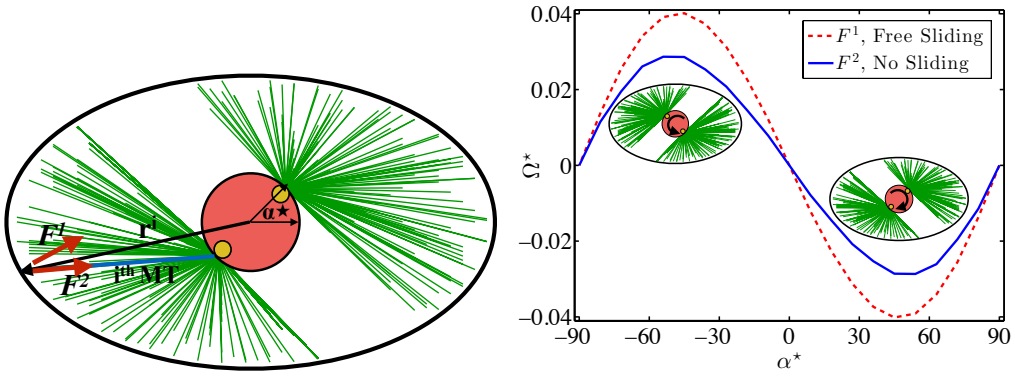

(a) Schematic of the simplified cortical pushing model (b) Angular velocity vs alignment angle

Figure 6: *(a) A schematic presentation of the simple cortical pushing model used only to demonstrate the minimum physics required to achieve torque instability in cortical pushing mechanism. (b) The dimensionless angular velocity vs the angle of intercentrosomal axis with AP-axis ($\alpha^\star$).*

These two variations of force are simple representations of free-sliding (force normal to the cortex) and no-sliding (force in the opposite direction of the tangent of the MT). The net torque on the PNC is computed by summing the torque induced by the end-forces on the individual MTs:

$$\mathbf{T} = \sum_{i=1}^{N} \mathbf{r}_i \times \mathbf{F}_i(L_i)$$

where $\mathbf{r}_i$ is the vector connecting the center of the PNC to the plus-end of the i^{th} MT. Note that this simple model does not contain the dynamic instability of MTs, any detailed hydrodynamic interactions (HIs), or

MT flexibility. In both models we take the drag coefficient of the PNC and the attached MTs, γ, to remain constant with the change of $\alpha^\star$.

Figure 6(b) shows the dimensionless angular velocity, $\Omega^\star = \Omega/\Omega_0$, as a function of $\alpha^\star$ where $\Omega_0 = \frac{\lambda E N}{8\pi\eta a_{PNC}^4}$. The results clearly show that although the net torque is zero at $\alpha^\star = -90$ and 90, infinitely small fluctuations induce a net torque that rotates the PNC towards the AP axis in a positive feed-back loop. On the contrary when the PNC is rotated away form the AP, a net torque is generated to realign the structure with the AP axis. Also the predictions from both variations of cortical forces are quantitatively close, which suggest that very slow rotation of the PNC in our detailed free-sliding model is not induced by the angle that the force is applied.

5 Cytoplasmic flows are generic features of active mechanisms

To demonstrate that the observed flow signatures are generic to each active mechanism, we present the results of our simulations for different values of of biophysical parameters that the ones presented in main text. As an example, in Fig. 7 we present the snapshots of the cytoplasmic flows in the no-sliding submodel in the early stages of migration (top), after centering (middle) and after rotation (bottom) for two values for the minimum rate of catastrophe ($f_{min} = 0.10\,\mathrm{s}^{-1}$ and $0.20\,\mathrm{s}^{-1}$) in cortical pushing model outlined in §2, with $f_{min} = 0.20$ corresponding the results presented in the main text.

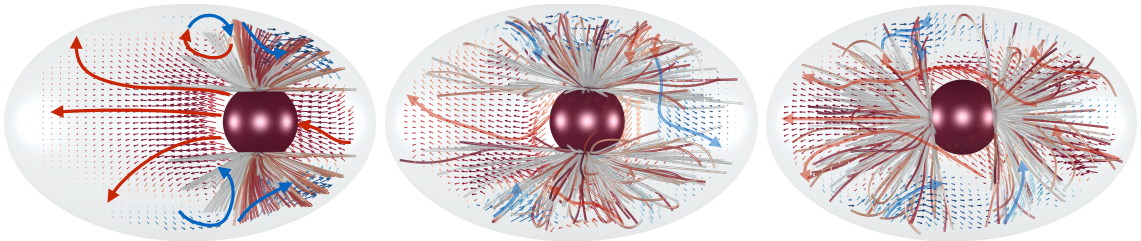

(a) $f_{min} = 0.10\,\mathrm{s}^{-1}$

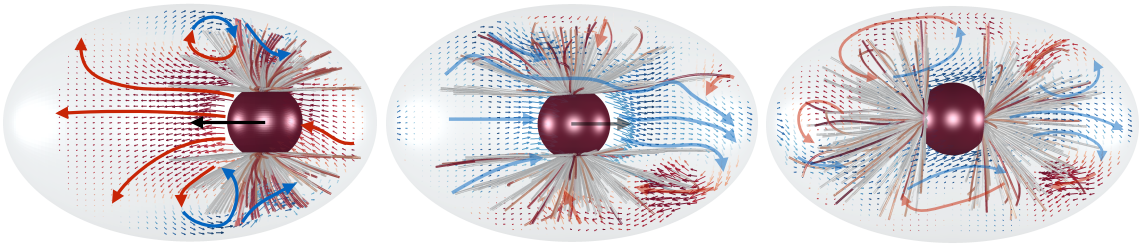

(b) $f_{min} = 0.20\,\mathrm{s}^{-1}$

Figure 7: *Snapshots of the simulated cytoplasmic flows in the initial stages of migration, after centering, and rotation of PNC in cortical pushing with the no-sliding motion sub-model for two different turnover time of the MTs growing against the cortex : (a) $f_{min} = 0.10\,\mathrm{s}^{-1}$, and (b) $f_{min} = 0.20\,\mathrm{s}^{-1}$.*

The snapshots clearly show that as a consequence of decreased rate of catastrophe (resulting in increasing contact time of MTs with the cell periphery) the MTs are substantially more deformed at $f_{min} = 0.10\,\mathrm{s}^{-1}$ compared with $f_{min} = 0.20\,\mathrm{s}^{-1}$ (Movies S3 and S5). The rotation time of PNC for $f_{min} = 0.10\,\mathrm{s}^{-1}$ was found to be roughly half of the rotation time of PNC with $f_{min} = 0.20\,\mathrm{s}^{-1}$, while the centering times in these two variations remained roughly unchanged (not shown here). Despite these evident changes in the dynamics of the PNC migration and the shape of the MTs, the generated flow signatures remain unchanged with this

change in the rate of catastrophe. Recall that these features for no sliding sub-model are strong flows near the cortex in the direction of the MTs and in the opposite direction of polymerization.

6 Centering through the cortical pulling mechanism depends on the choice of model parameters

As mentioned in the main text, unlike the other two mechanisms, in the cortical pulling model the pronuclear centering is only achieved in a narrow range of parameters of the model used in this study. These parameters include the total number of cortically bound dyneins, the rate of detachment of captured MTs from cortically bound dyneins, and the slope by which the density of the cortically bound dyneins on the posterior side decrease from the pole to the dividing plane of the cell. Here we give few examples of failed centration of the PNC.

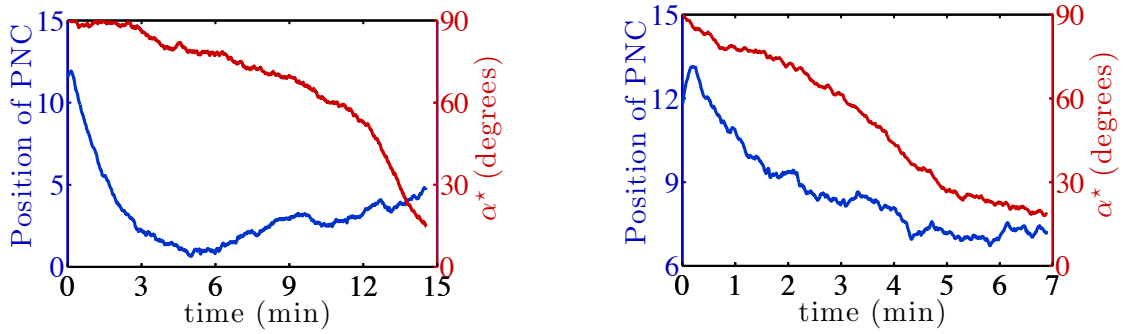

(a) Larger number of motors

(b) Slower detachment rates

Figure 8: *Two cases where the cortical pulling model does not center the PNC: (a) the number of cortical dynein motors are doubled with respect to the case of properly centered PNC in the main tex; and (b) the rate of detachment is increased a factor of 2.*

For example, when the number of the cortically bound dynein motors is increased from 100 to 200, the PNC initially migrates towards the center. However, at later times the PNC moves back to the posterior side of the cell. Despite failure of centering, the intercentrosomal axis of PNC rotates and properly aligns with the AP-axis. These results are presented in figure 8(a).

In another example shown in figure 8(b), we increase the rate of detachment from 0.3 $(1/\text{min})$ to 0.6 $(1/\text{min})$. While the intercentrosomal axis successfully aligned with the AP axis, the PNC remained in the posterior side of the cell.

Changing the spatial variation of the cortical dyneins also resulted in failed centering, and successful rotation which are not shown here. It seems that this particular choice of model for cortical pulling mechanism allows multiple statistically stable solutions subjected to zero net force on the PNC, while other active mechanisms are not present. Our results suggest that the final position of the PNC depends critically on the competition between the different time-scales in this problem, which include the average time it takes MTs to grow to the cortex, the time the MTs remain attached to the cortex, and the time scale of migration.

References

DANIELS, B. R., MASI, B. C. & WIRTZ, D. 2006 Probing single-cell micromechanics in vivo: the microrheology of C. elegans developing embryos. *Biophys. J.* **90** (12), 4712–4719.

DOGTEROM, M. & YURKE, B. 1997 Measurement of the force-velocity relation for growing microtubules. *Science* **278** (5339), 856–860.

VAN DOORN, G. S., TANASE, C., MULDER, B. M. & DOGTEROM, M. 2000 On the stall force for growing microtubules. *Eur. Biophys. J.* **29** (1), 2–6.

GÖNCZY, P., PICHLER, S., KIRKHAM, M. & HYMAN, A. A. 1999 Cytoplasmic dynein is required for distinct aspects of mtoc positioning, including centrosome separation, in the one cell stage caenorhabditis elegans embryo. *The J. Cell Biol.* **147** (1), 135–150.

GÖTZ, T. 2000 *Interactions of fibers and flow: asymptotics, theory and numerics*. dissertation.

GREENGARD, L. & ROKHLIN, V. 1987 A fast algorithm for particle simulations. *Journal of computational physics* **73** (2), 325–348.

GRILL, S. W., HOWARD, J., SCHÄFFER, E., STELZER, E. H. & HYMAN, A. A. 2003 The distribution of active force generators controls mitotic spindle position. *Science* **301** (5632), 518–521.

HOWARD, J. 2001 *Mechanics of Motor Proteins and the Cytoskeleton*, 1st edn. Sinauer Associates, Inc.

JANSON, M. E., DE DOOD, M. E. & DOGTEROM, M. 2003 Dynamic instability of microtubules is regulated by force. *J. Cell Biol.* **161** (6), 1029–1034.

JOHNSON, R. E. 1980 An improved slender-body theory for Stokes flow. *Journal of Fluid Mechanics* **99** (02), 411.

KELLER, J. & RUBINOW, S. 1976 Slender-body theory for slow viscous flow. *Journal of Fluid Mechanics* **75**, 705–714.

KIMURA, A. & ONAMI, S. 2005 Computer simulations and image processing reveal length-dependent pulling force as the primary mechanism for C. elegans male pronuclear migration. *Dev. Cell* **8** (5), 765–775.

KIMURA, A. & ONAMI, S. 2007 Local cortical pulling-force repression switches centrosomal centration and posterior displacement in C. elegans. *J. Cell Biol.* **179** (7), 1347–1354.

KIMURA, K. & KIMURA, A. 2011 Intracellular organelles mediate cytoplasmic pulling force for centrosome centration in the Caenorhabditis elegans early embryo. *Proc. of the National Academy of Sciences of the United States of America* **108** (1), 137–142.

MCNALLY, F. J. 2013 Mechanisms of spindle positioning. *J. Cell Biol.* **200** (2), 131–140.

NAZOCKDAST, E., RAHIMIAN, A., ZORIN, D. & SHELLEY, M. 2016 Fast and high-order methods for simulating fiber suspensions applied to active cellular mechanics. *arXiv:1602.05650 [math.NA]* .

NAZOCKDAST, E., RAHIMIAN, A., ZORIN, D. & SHELLEY, M. J. 2017 A fast platform for simulating semi-flexible fiber suspensions applied to cell mechanics. *Journal of Computational Physics* **329**, 173–209.

POWER, H. & MIRANDA, G. 1987 Second Kind Integral Equation Formulation of Stokes' Flows Past a Particle of Arbitrary Shape. *SIAM Journal on Applied Mathematics* **47** (4), 689.

POZRIKIDIS, C. 1992 *Boundary Integral and Singularity Methods for Linearized Viscous Flow*. Cambridge University Press.

REDEMANN, S., PECREAUX, J., GOEHRING, N. W., KHAIRY, K., STELZER, E., HYMAN, A. A. & HOWARD, J. 2010 Membrane invaginations reveal cortical sites that pull on mitotic spindles in one-cell c. elegans embryos. *PLoS One* **5** (8), e12301–e12301.

SAAD, Y. & SCHULTZ, M. H. 1986 Gmres: A generalized minimal residual algorithm for solving nonsymmetric linear systems. *SIAM J. Sci. Stat. Comput.* **7** (3), 856–869.

SHINAR, T., MANA, M., PIANO, F. & SHELLEY, M. J. 2011 A model of cytoplasmically driven microtubule-based motion in the single-celled Caenorhabditis elegans embryo. *Proc. Natl. Acad. Sci. USA* **108** (26), 10508–10513.

TORNBERG, A.-K. & SHELLEY, M. J. 2004 Simulating the dynamics and interactions of flexible fibers in Stokes flows. *Journal of Computational Physics* **196** (1), 8–40.

TSOU, M.-F. B., HAYASHI, A., DEBELLA, L. R., MCGRATH, G. & ROSE, L. S. 2002 LET-99 determines spindle position and is asymmetrically enriched in response to PAR polarity cues in C. elegans embryos. *Development (Cambridge, England)* **129** (19), 4469–4481.

YING, L., BIROS, G. & ZORIN, D. 2004 A kernel-independent adaptive fast multipole algorithm in two and three dimensions. *Journal of Computational Physics* **196** (2), 591–626.